nature geoscience

Article

https://doi.org/10.1038/s41561-025-01684-6

Extreme Indian summer monsoon states stifled Bay of Bengal productivity across the last deglaciation

Received: 14 March 2024

Accepted: 26 March 2025

Published online: 28 April 2025

Check for updates

K. Thirumalai[1] ✉, S. C. Clemens[2], Y. Rosenthal[3], S. Conde[1], K. Bu[3], S. Desprat[4,5], M. Erb[6], L. Vetter[1], M. Franks[1], J. Cheng[7,8], L. Li[7], Z. Liu[7], L. P. Zhou[9], L. Giosan[10,11], A. Singh[12] & V. Mishra[13]

Indian summer monsoon (ISM) hydrology fuels biogeochemical cycling across South Asia and the Indian Ocean, exerting a first-order control on food security in Earth's most densely populated areas. Although the ISM is projected to intensify under continued greenhouse forcing, substantial uncertainty surrounds anticipating its impacts on future Indian Ocean stratification and primary production—processes key to the health of already-declining fisheries in the region. Here we present century-scale records of ISM runoff variability and marine biogeochemical impacts in the Bay of Bengal (BoB) since the Last Glacial Maximum (~21 thousand years ago (ka)). These records reveal extreme monsoon states relative to modern strength, with weakest ISM intensity during Heinrich Stadial 1 (~17.5–15.5 ka) and strongest during the early Holocene (~10.5–9.5 ka). Counterintuitively, we find that BoB productivity collapsed during *both* extreme states of peak monsoon excess and deficits—both due to upper-ocean stratification. Our findings point to the possibility of future declines in BoB primary productivity under a strengthening and more variable ISM regime.

In addition to Indian summer monsoon (ISM) rainfall being the prime source of freshwater for much of the Indian subcontinent, monsoon dynamics and riverine discharge profoundly affect marine ecosystems across the northern Indian Ocean, a region where fisheries are closely tied to primary production[1,2]. Coastal populations of the subcontinent are among the planet's densest and most vulnerable, subsisting primarily on marine-derived protein sources[3]. Thus, addressing how ISM variability and its impacts on marine biogeochemical cycling will respond to global change is integral for appraisals of future food security across South Asia[2,3].

The latest generations of global climate simulations, including the Coupled Model Intercomparison Project version 6 (CMIP6), converge regarding the future thermodynamical strengthening of ISM rainfall[4,5]. Yet substantial disagreement exists regarding the biogeochemical response of the northern Indian Ocean under greenhouse warming according to Earth-system models[6]. These models simulate future

[1]Department of Geosciences, University of Arizona, Tucson, AZ, USA. [2]Department of Earth, Environmental and Planetary Sciences, Brown University, Providence, RI, USA. [3]Department of Marine and Coastal Sciences and Department of Earth and Planetary Science, Rutgers, State University of New Jersey, New Brunswick, NJ, USA. [4]Environnements et Paléoenvironnements Océaniques et Continentaux (EPOC), University of Bordeaux, CNRS, EPHE, UMR 5805, Pessac, France. [5]EPHE, PSL University, Paris, France. [6]School of Earth and Sustainability, Northern Arizona University, Flagstaff, AZ, USA. [7]Department of Geography, Ohio State University, Columbus, OH, USA. [8]School of Marine Sciences, Nanjing University of Information Science and Technology, Nanjing, China. [9]Laboratory for Earth Surface Processes, Department of Geography and Institute of Ocean Research, Peking University, Beijing, China. [10]STAR Institute, Babeș-Bolyai University, Cluj-Napoca, Romania. [11]Research Institute of the University of Bucharest (ICUB), Bucharest, Romania. [12]Physical Research Laboratory, Navrangpura, Ahmedabad, India. [13]Civil Engineering, Indian Institute of Technology Gandhinagar, Gandhinagar, India. ✉e-mail: kaustubh@arizona.edu

https://doi.org/10.1038/s41561-025-01684-6

reductions in net primary productivity[7] and nutrient inventory[6] in the Arabian Sea, whereas projections remain highly uncertain for the Bay of Bengal (BoB), disagreeing even on the sign of change[6,7]. Field studies indicate that primary production in the BoB is boosted by near-coastal eddy pumping and energetic mixing[8–10] and is impeded by seasonal barrier-layer stratification that inhibits mixing and nutrient transport from depth[10,11]. The lack of long-term, in situ biogeochemical observations[8–10] further precludes our ability to inform our understanding of future changes alongside simulations[6].

Here we provide palaeoceanographic perspectives on the interaction between summer monsoon runoff, stratification and marine primary productivity in the BoB over the past ~22,000 years (~22 kiloannum before 1950 CE; hereafter ka). We focus on the interval from the Last Glacial Maximum (LGM; ~23–19 ka) through the Holocene (11.7 ka–present), representing the most recent geological interval of sustained global warming. ISM runoff and marine biogeochemical variability in the northwest BoB were reconstructed using foraminiferal tests from sediments drilled at International Ocean Discovery Program (IODP) Site U1446 (Fig. 1; 19.08° N, 85.73° E; 1,430 m water depth). Site U1446 is in the central path of the East India Coastal Current (EICC), a seasonally reversing boundary current bringing Ganges–Brahmaputra–Meghna (GBM) outflow equatorward during the post-monsoon season, inducing sea surface salinity (SSS) minima during October and November (Fig. 1). The volume of seasonal GBM discharge, driven by the intensity of ISM runoff, modulates annual SSS variability of EICC waters[12–15]. We infer past EICC SSS variations by reconstructing the stable oxygen isotope composition of seawater ($\delta^{18}O_{sw}$; reported relative to Vienna Standard Mean Ocean Water (VSMOW)) at Site U1446 (Extended Data Figs. 1 and 2 and Methods). Using indicators of past water-column biogeochemistry, we uncover a nonlinear relationship between ISM intensity and primary production in the BoB since the LGM.

Reconstructing monsoonal outflow and ocean biogeochemistry

We reconstructed $\delta^{18}O_{sw}$ as a proxy for ISM runoff at IODP Site U1446 using planktic foraminiferal geochemistry. Our study focuses on the top ~7 m of sediments cored at this site, which contains a robust age model constrained by 14 radiocarbon measurements (Methods and Extended Data Fig. 3). We analysed the stable oxygen isotope composition in calcite tests ($\delta^{18}O_c$; reported relative to Vienna Pee Dee Belemnite(VPDB)) of planktic foraminifer, *Globigerinoides ruber* (white variety; ~70–90 tests per multi-specimen analysis). This species lives year-round in BoB surface waters[16], and its $\delta^{18}O_c$ is controlled by sea surface temperature (SST) and $\delta^{18}O_{sw}$ at the time of calcification. We also measured magnesium-to-calcium (Mg/Ca) ratios as an independent proxy for past SST variability. We then used an iterative approach[17] with locally validated calibration equations[18] to calculate SST and local changes in $\delta^{18}O_{sw}$ (hereafter $\delta^{18}O^*_{sw}$; Methods), which were calculated by correcting for average oceanic $\delta^{18}O_{sw}$ variations due to global ice-volume fluctuations (Methods). Accordingly, we infer reconstructed local changes in $\delta^{18}O_{sw}$ ($\delta^{18}O^*_{sw}$; a proxy for salinity[17]) at Site U1446 as variability in ISM runoff intensity.

We analysed planktic foraminiferal assemblages and trace element ratios (Cd/Ca, U/Ca) in *G. ruber* tests to assess past productivity and nutrient inventory in the surface ocean at Site U1446. We focused on the relative abundance of *Globorotalia* species as a proxy for export productivity (Methods). *G. ruber* Cd/Ca reflects dissolved cadmium in the surface ocean[19], which strongly correlates with the concentration of the macronutrient phosphorus[19,20]. Although the northern BoB is limited by nitrogen rather than by phosphorus[10], we submit that elevated *G. ruber* Cd/Ca ratios correspond not only to an increase in phosphorus but also other related nutrients (for example, nitrate) sourced from depth during intervals of higher primary production. We infer *G. ruber* U/Ca to be driven by diagenetic processes modulated

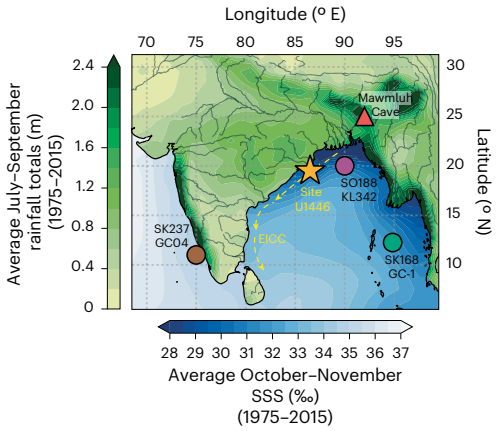

Fig. 1 | Site locations and ISM rainfall and post-monsoon salinity. June–September monthly mean precipitation (brown-to-green) with October–November salinity (blue-to-white) in the Indian monsoon domain. Proxy sites include Site U1446 (star, this study), Mawmluh Cave[45] (triangle) and sediment cores (circles) SK168[35], SK237-GC04[29] and SO188-KL342[32]. Precipitation was taken from the Global Precipitation Climatology Centre (GPCC) dataset[46] and salinity from the Ocean Reanalysis System 4 (ORA-S4) reanalysis dataset[47].

by changes in organic matter flux or bottom water oxygen levels[21,22]. Considering minimal-to-no evidence for deepwater anoxia over this interval[23], we surmise that low *G. ruber* Cd/Ca and U/Ca at Site U1446 and low abundances of *Globorotalia* were associated with reduced BoB primary productivity driven by a lack of nutrients delivered to the photic zone.

Finally, we investigated past seasonal variability of the upper water column at Site U1446 by performing stable isotopic individual foraminiferal analyses (IFA) on three depth-stratified species of planktic foraminifera: *G. ruber* (White), *Trilobatus sacculifer* and *Neogloboquadrina dutertrei* (Table 1 and Methods). These taxa were selected due to their distinct median calcification depths[24], which we locally estimate to be ~10–30 m, ~15–45 m and ~40–60 m depth, respectively, based on comparisons with observations (Extended Data Fig. 4). Forward modelling of IFA-$\delta^{18}O_c$ at our site shows that cold-season temperatures push the distribution towards more positive values[14]. In contrast, monsoonal GBM discharges skew the distribution towards more negative values. We expect substantial differences in median IFA-$\delta^{18}O_c$ and -$\delta^{13}C_c$ values between the surface-ocean (*G. ruber* & *T. sacculifer*) and subsurface (*N. dutertrei*) taxa during times of sharp density stratification in the upper water column.

Indian palaeomonsoon runoff since the LGM

The $\delta^{18}O^*_{sw}$ record at IODP Site U1446 indicates that modern ISM runoff intensity was intermediate to that of extreme palaeomonsoon states over the past 22,000 years (Fig. 2b). Agreement between observed $\delta^{18}O_{sw}$ and SST with reconstructed core-top values across multiple core locations (Fig. 2a,b,f,h) provides confidence in our chosen calibrations and quantitative interpretations of BoB palaeoceanography. LGM $\delta^{18}O^*_{sw}$ at Site U1446 is significantly higher than modern values (by ~0.45 ‰ VSMOW) and corresponds to ~20% reduced runoff seasonality (based on the regression depicted in Extended Data Fig. 2). Maximum $\delta^{18}O^*_{sw}$ (~0.50 ‰) values occur during Heinrich Stadial 1 (HS1; 17–16 ka), suggesting an ~50% reduction (Extended Data Fig. 2) compared to modern seasonality. We note that such positive seawater $\delta^{18}O$ values are only observed today in the far southern BoB[12] and are associated with high SSS conditions (≥ 35‰). Such magnitudes in the coastal northwest BoB are consistent with a scenario of halted riverine input into the BoB using a high-resolution ocean model[25], in addition to the transient TraCE21ka simulation[26] of HS1 (Methods and Extended Data Figs. 5–7). Runoff then intensified over the deglaciation, albeit with

https://doi.org/10.1038/s41561-025-01684-6

Table 1 | Multi-species IFA and reconstructed water column properties at Site U1446 with 1σ uncertainty propagation performed using PSU Solver

Species	Multi-specimen Mg/Ca[a]	IFA (n)	Mean IFA-$\delta^{18}O_c$	1σ IFA-$\delta^{18}O_c$	Mean IFA-$\delta^{13}C_c$	1σ IFA-$\delta^{13}C_c$	Estimated T±1σ (°C)	Estimated $\delta^{18}O_{sw}$±1σ (‰)[b]	Estimated S±1σ (‰)
Late Holocene (1–0 ka)									
G. ruber	4.41	48	−2.54	0.36	1.48	0.39	27.0±0.6	−0.4±0.13	32.2±0.9
T. sacculifer	4.24	75	−2.51	0.28	1.82	0.44	26.7±0.5	−0.2±0.12	32.7±0.8
N. dutertrei	2.73	98	−1.86	0.32	1.28	0.50	26.4±0.6	0.5±0.12	33.8±0.8
Early Holocene (10–9 ka)									
G. ruber	4.31	47	−2.85	0.69	1.16	0.53	27.5±0.6	−0.9±0.12	31.0±0.8
T. sacculifer	4.17	60	−2.73	0.58	1.65	0.39	27.4±0.6	−0.9±0.13	30.8±0.9
N. dutertrei	2.55	58	−1.63	0.23	0.29	0.33	25.7±0.5	0.3±0.13	32.5±0.9
Heinrich Stadial 1 (17–16 ka)									
G. ruber	4.53	40	−1.11	0.33	1.15	0.49	26.3±0.6	0.5±0.13	34.7±0.9
T. sacculifer	4.15	59	−0.47	0.28	1.75	0.34	25.8±0.5	0.5±0.12	34.8±0.8
N. dutertrei	2.27	63	−0.16	0.28	0.37	0.36	24.6±0.6	0.8±0.13	36.0±0.9

Inversions were performed using PSU Solver applying the Gray et al. (2018) framework of equations[43] for paired Mg/Ca–$\delta^{18}O$; note that early Holocene and Heinrich Stadial 1 calculations of $\delta^{18}O^*_{sw}$ were performed with a global $\delta^{18}O_{sw}$ correction[17] using a deglacial-specific sea-level curve[44]. The same routine was employed for all species. σ, 1σ error on the mean value based on the number of IFA measurements, incorporating analytical errors. *T*, estimated calcification temperature; *S*, estimated calcification salinity. [a]Multi-specimen Mg/Ca analysis was performed using 60–90 crushed and pooled tests taken from the 400–500 µm size fraction (same as for IFA; Methods). [b]‰ reported relative to Vienna Standard Ocean Mean Water (SMOW).

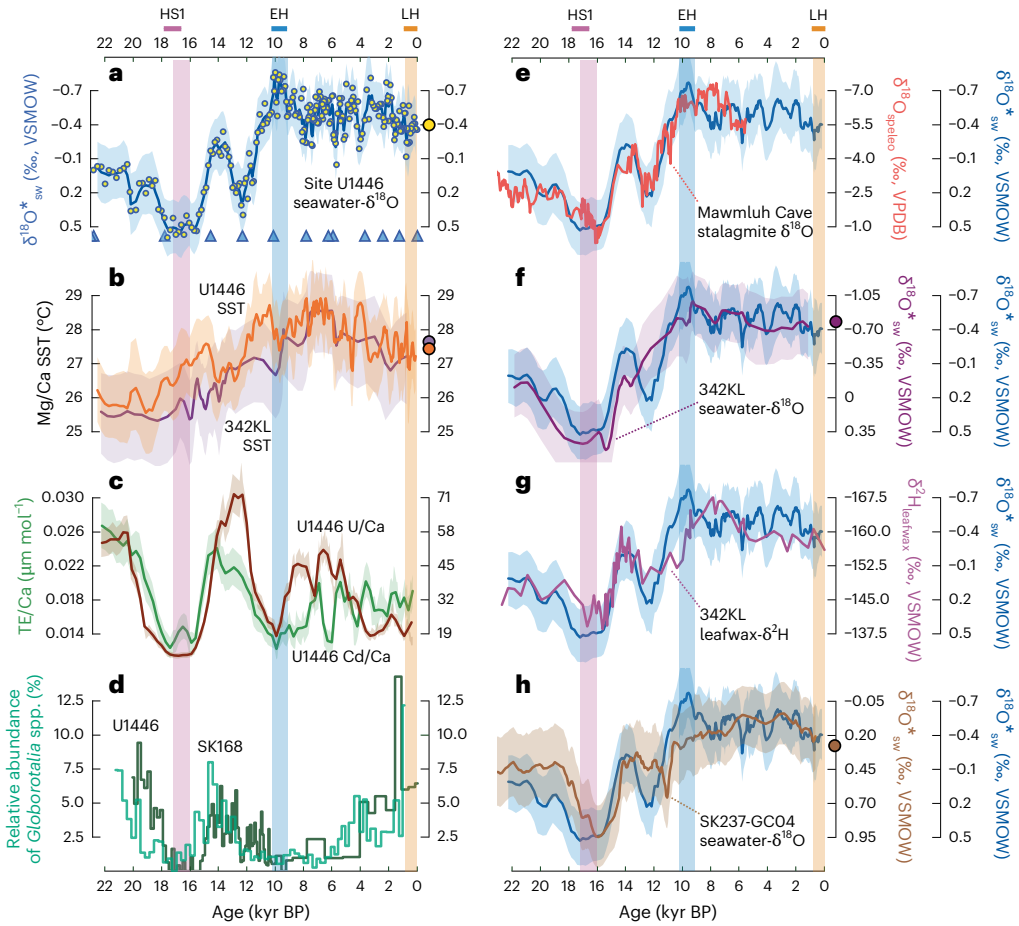

Fig. 2 | Palaeoceanographic records from the BoB and Indian palaeomonsoon reconstructions since the Last Glacial Maximum. a, Reconstructed $\delta^{18}O^*_{sw}$ at Site U1446 (that is, local variations in seawater $\delta^{18}O$ corrected for changes in global ice volume; circles) using paired Mg/Ca-$\delta^{18}O_c$ measurements in *G. ruber* tests as a proxy for ISM runoff, with 3-point centred running-mean (thick line), its ± 1σ uncertainty (envelope, calculated with ref. 17) and radiocarbon ages (triangles). **b**, Reconstructed SST and its uncertainty (± 1σ derived from inversion using PSU Solver[17]) at Site U1446 and SO188-KL342[32]. **c**, Cd/Ca and U/Ca variations in *G. ruber* at Site U1446 (± 1σ depicted is analytical uncertainty; Methods). TE, trace elemental. **d**–**h**, Relative planktic foraminiferal species abundances of genus *Globorotalia* at Site U1446 and SK168[35] in the Andaman Sea (**d**) and comparisons of Site U1446 $\delta^{18}O^*_{sw}$ with Mawmluh Cave[45] speleothem $\delta^{18}O$ (**e**), SO188-KL342[32] $\delta^{18}O^*_{sw}$ (**f**) and leaf-wax[48] δ^2H (**g**) and SK237-GC04[29] $\delta^{18}O^*_{sw}$ (**h**). All thick lines depict 3-point centred running means on proxy data with associated uncertainty envelopes (except for species abundances depicted in **d**); modern observations of $\delta^{18}O_{sw}$ and SST are depicted directly on axes. Details regarding uncertainty propagation and calibration equations used in calculating $\delta^{18}O^*_{sw}$ can be found in the Methods. The LH (1–0 ka), EH (10–9 ka) and HS1 (17–16 ka)—intervals of focus for subsequent analyses—are highlighted. kyr BP, thousands of years before present (1950)—equivalent to ka.

https://doi.org/10.1038/s41561-025-01684-6

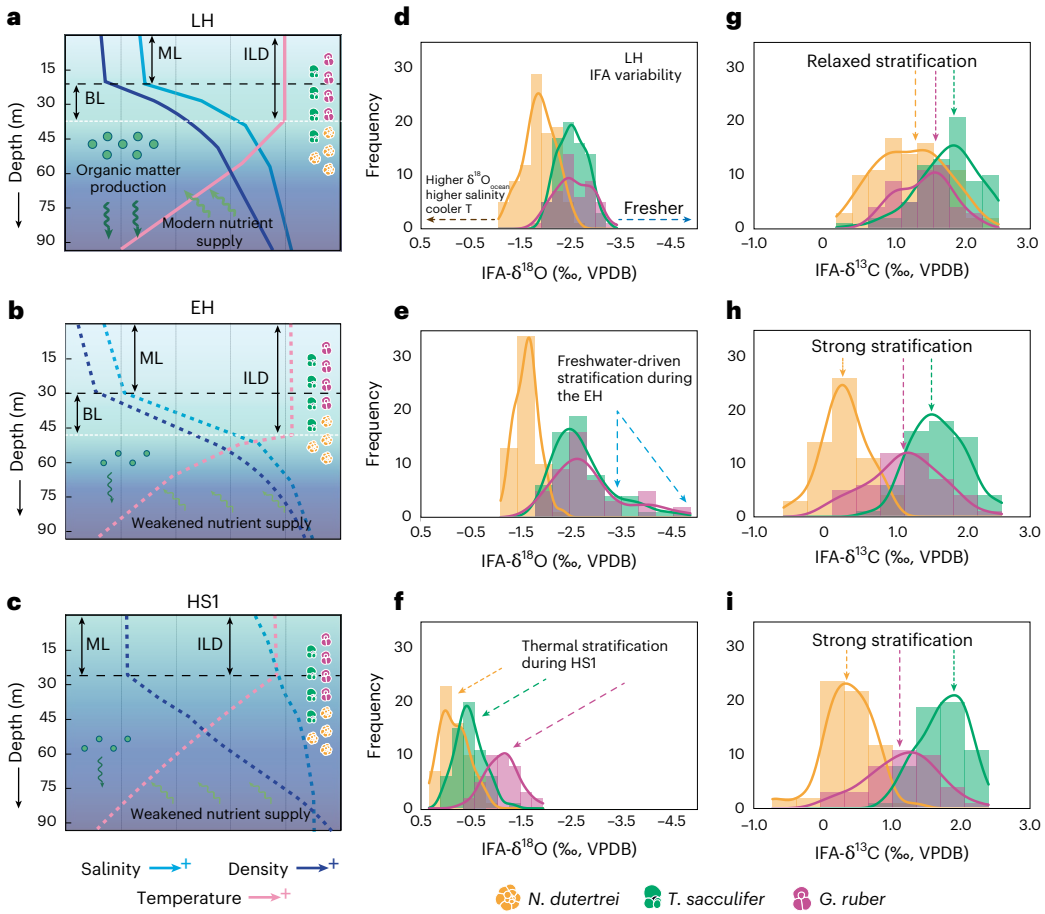

Fig. 3 | Mechanisms of upper-ocean stratification in the BoB and impacts on primary production inferred from foraminiferal geochemistry. **a**–**c**, Depth-profile schematic of inferred mean-annual temperature (pink), salinity (blue) and density (dark blue) depicting hypothesized mechanism linking runoff, nutrient delivery, barrier-layer dynamics and impacts on palaeoproductivity in the BoB during the LH (**a**), EH (**b**) and HS1 (**c**) intervals, where mixed-layer (ML) depth, isothermal layer depth (ILD) and barrier-layer (BL) depth are delineated. Solid lines are hydrographic profiles based on conductivity-depth-temperature observations; dashed lines are hypothesized profiles for the studied palaeo-intervals. **d**–**i**, Histograms of individual foraminiferal analyses (IFA) for the stable oxygen (IFA-$\delta^{18}O_c$) (**d**–**f**) and carbon (IFA-$\delta^{13}C_c$) isotope composition (**g**–**i**) measured in the calcite tests of three different species (*G. ruber*—pink, *T. sacculifer*—teal and *N. dutertrei*—yellow). Each row corresponds to a different time period. LH profiles were based on observed conductivity-depth-temperature profiles proximal to Site U1446. Inferred calcifying depth habitats of *G. ruber*, *T. sacculifer* and *N. dutertrei* are also shown.

millennial-scale fluctuations during the Bølling–Allerød and Younger Dryas periods (Fig. 2a). The millennial-scale $\delta^{18}O^*_{sw}$ structure reaffirms the linkage between ISM precipitation and deglacial climate anomalies in the North Atlantic owing to meridional circulation changes, as has been posited elsewhere[27,28]. After the deglaciation, we find that ISM runoff peaked during the early Holocene (EH; 10.5–9.5 ka), an interval with extremely low $\delta^{18}O^*_{sw}$ (approximately −0.85‰ VSMOW) values corresponding to ≥ 30% intensification of ISM seasonality. Then, ISM runoff steadily declined from 10–8 ka and experienced pronounced (multi-)centennial-scale variability with abrupt deficits punctuating steady ISM runoff at ~5.8 ka, ~4 ka, ~2 ka and during ~0.7 ka. Late Holocene (LH) $\delta^{18}O^*_{sw}$ values at Site U1446 are intermediate (−0.4 ± 0.1‰ VSMOW) to those during HS1 (0.5 ± 0.1‰) and EH (−0.8 ± 0.1‰) intervals, indicating that ISM runoff over the past 22,000 years was both much weaker and much stronger than modern intensity (Figs. 2–4).

ISM variations since the LGM inferred from Site U1446 $\delta^{18}O^*_{sw}$ are consistent with other well-resolved marine and terrestrial hydroclimate records in the region. An absolutely dated speleothem $\delta^{18}O$ record from Mawmluh Cave in Meghalaya, India, matches the deglacial timing and phasing of $\delta^{18}O^*_{sw}$ variability at Site U1446 (Fig. 2e), supporting the chronology of the marine record, and suggesting a robust coupling between changes in the isotopic composition of rainwater over northeastern India and GBM runoff over this interval (Fig. 2e). Reconstructed $\delta^{18}O^*_{sw}$ and leaf-wax-δD from a northern BoB site (SO188-KL342), outside the EICC region, are also consistent with ISM variations inferred from Site U1446 $\delta^{18}O^*_{sw}$ (Fig. 2f,g). Additionally, SST reconstructions at both sites show similar evolution from the LGM to the present (Fig. 2b). A $\delta^{18}O^*_{sw}$ record from offshore the Malabar Coast[29], thought to be sensitive to runoff from the Western Ghats, also indicates weakened runoff during HS1 but diverges from the northern BoB records and suggests minimal change between the EH and LH intervals (Fig. 2h). The lack of low $\delta^{18}O^*_{sw}$ at the Malabar site during the EH may be due to higher rainfall in the GBM catchment relative to the Western Ghats or due to the advection of water masses moving northwestward past the tip of southern India, influenced by peninsular runoff associated with the northeastern monsoon[30]. Nevertheless, we find broad agreement within regional records for increasing ISM runoff across the last deglaciation, with peak ISM runoff during the EH and weakest intensity during HS1 relative to modern ISM variability.

Monsoon impact on marine productivity

Coeval reconstructions of SST, ISM runoff, marine productivity and nutrient delivery to the upper ocean allow us to diagnose monsoon–biogeochemical linkages in the northwest BoB since the LGM (Fig. 3). We

https://doi.org/10.1038/s41561-025-01684-6

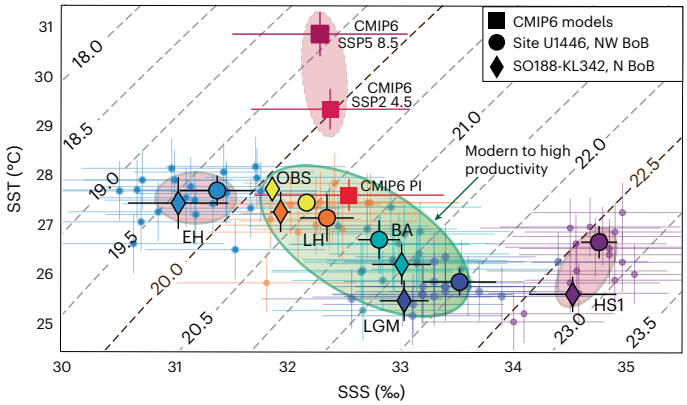

Fig. 4 | Past, present and future density of surface waters in the northern BoB. Temperature–salinity (*T*–*S*) isopycnals constructed at Site U1446 (circles) and core site SO188-KL342[32] (diamonds) with values from observations (OBS; yellow) and estimated values for palaeointervals using paired *G. ruber* Mg/Ca-$\delta^{18}O$ (symbols without borders are estimates from individual samples; symbols with borders depict median values): LH (0.7–0 ka), EH (10–9 ka), Bølling–Allerød (BA; 14.5–13.5 ka), HS1 (17–16 ka) and the LGM (21–20 ka). Simulations (squares); pre-industrial (PI; $n = 34$ models; Methods), Shared Socioeconomic Pathways (SSP) scenarios 2 (SSP2–4.5; $n = 33$ models) and 5 (SSP5–8.5; $n = 34$ models). Isopycnals were constructed with the Python Seawater package. Error bars on individual temperature and salinity estimates for the palaeointervals (thin lines) were calculated using the proxy system model PSU Solver[17] for each sample, whereas errors on the median values (thick lines) are ± 1σ values calculated from individual measurements and their uncertainty ($n > 12$ for each interval). Error bars on simulations (coloured lines on squares) represent the ± 1σ variability between various model simulations from a given scenario based on the number of models listed above (Methods). Green ellipse depicts intervals of high productivity in the northern BoB according to our reconstructions where brown ellipses suggest deteriorations in productivity. All markers in the above plot are depicted using the median as the central measure.

find that both nutrient delivery and organic matter export fluxes were higher relative to modern values during the LGM, when monsoon seasonality was subdued and SSTs were ~1.5 °C cooler than present (Figs. 2 and 4), in agreement with other reconstructions from the BoB[31,32]. This finding is consistent with longer-term Pleistocene investigations that found lowered BoB productivity during interglacials relative to glacial periods when higher freshwater outflow limited vertical mixing via stratification[33], although we note that spatial and seasonal variability may exist across areas of the northern Indian Ocean[34]. In contrast, during HS1, when ISM runoff was at its lowest, we find that *Globorotalia* populations plummeted at Site U1446 and nearly vanished (Fig. 2d), alongside the lowest *G. ruber* Cd/Ca and U/Ca values (Fig. 2c). This reduction in *Globorotalia* populations is also observed in the record from Core SK168[35] in the Andaman Sea (Fig. 1), whose subsequent trends mirror those observed at Site U1446.

After HS1, upper-ocean nutrients and productivity in the northwestern BoB increased until ~12.5 ka, during the transition from the Bølling–Allerød to the Younger Dryas. Then, as ISM runoff increased towards its peak at ~10.5–9.5 ka, we find that *G. ruber* Cd/Ca and U/Ca and *Globorotalia* populations plunge towards HS1 magnitudes (Fig. 2d). Over the Holocene, the biogeochemical indicators show more minor yet distinct fluctuations which are more challenging to interpret—there is a noticeable decoupling between U/Ca and the relative abundance of *Globorotalia* around ~5 ka. This may arise due to the advection of well-oxygenated bottom water masses in the Holocene[36], which could limit sedimentary U generation and lower U/Ca sensitivity towards primary productivity in the water column[21]. However, relative to the LH interval, our findings collectively point to robust declines in particulate organic matter flux and nutrient delivery to the upper ocean in the coastal BoB during the EH and HS1.

Drivers of deglacial stratification

How can productivity losses occur during extreme palaeomonsoon excess and deficit? Under the modern oceanographic regime, post-monsoon outflow into the BoB induces a low-salinity mixed layer and a steep halocline, both overlying the thermocline and seated within the isothermal portion of the water column (Fig. 3a). The resultant formation of the barrier layer—spanning the depth between the onset of the halocline and the thermocline[11]—hinders mixing and lowers nutrient supply from depth due to stratification (Fig. 3a). Riverine runoff may bring silicate nutrients to the BoB, although, nearly all of the nitrogen and phosphorus is thought to be utilized in the estuarine zones, before reaching the interior BoB[37]. This biogeochemical configuration of the BoB may have been altered in the past—for example, peak deglacial nutrient concentrations coincide with freshwater inflow at ~14 ka (Fig. 2a), suggesting that fluvially delivered nutrients may have played a more prominent role. However, other processes exert a more substantial influence in modulating nutrient delivery, as signified by the decoupling between $\delta^{18}O^*_{sw}$ and Cd/Ca values during the EH. Under present-day conditions, seasonal barrier-layer erosion and coastal eddy pumping enhance macronutrient delivery to the upper ocean and are conducive to phytoplankton blooms in the BoB[38]. Local wind forcing and remote ocean–atmospheric energetics[39] can also promote eddies and thereby impact seasonal nutrient delivery to upper-ocean waters. Accordingly, episodes of strong vertical stratification in the upper waters of the BoB are observed to coincide with lowered primary production[1]. Using IFA applied to intervals of peak monsoon runoff (EH) and deficit (HS1) at Site U1446, we investigate upper-ocean stratification as a cause for decreased primary production during both intervals.

During the EH, IFA-$\delta^{18}O_c$ distributions for both mixed-layer species show highly skewed freshwater-driven tails relative to the LH histograms (Fig. 3d,e). This indicates strengthened seasonal ISM outflow[14], consistent with the independently derived multi-species $\delta^{18}O^*_{sw}$ estimates. Given virtually identical distributions for both mixed-layer species (teal and pink lines in Fig. 3e), we infer that greater ISM runoff induced a thicker barrier layer that suppressed upward nutrient advection into the photic zone via freshwater stratification; this led to reductions in primary production (Fig. 3b). Similar IFA-$\delta^{18}O_c$ ranges in LH and EH histograms for the subsurface-dwelling species, *N. dutertrei*, confirms their presence beneath the mean-annual barrier layer (Fig. 3b) during the EH and constrains the freshening to the surface ocean, imposed by GBM runoff conveyed to Site U1446 by the EICC. The TraCE21ka transient simulation indicates that the strongest ISM surface winds (Extended Data Fig. 5) and circulation (Extended Data Figs. 6 and 7) over the past 21 ka persisted under EH boundary conditions; this implies that the deep EH barrier layer caused by intensified ISM runoff was unable to be breached even under a strong ISM wind regime.

During HS1, we find that IFA-$\delta^{18}O_c$ values are unimodal for all three upper-ocean species (Fig. 3f), suggesting strong upper-water-column stratification. Paired Mg/Ca-$\delta^{18}O_c$ analyses in this interval show that temperature changes drive the IFA distributions (Table 1), supporting inferences from forward modelling[14]. The lack of overlap between *G. ruber* and *T. sacculifer* IFA-$\delta^{18}O_c$ during HS1 represents a departure from the LH and EH intervals (Fig. 3d,e), suggesting a pronounced shift in oceanographic regime relative to the Holocene. Providing a subsurface constraint, *N. dutertrei* IFA-$\delta^{18}O_c$ during HS1 suggests that calcification occurred under cooler and more saline water masses relative to LH and EH intervals and to the other species' distributions (Fig. 3f).

Additional support for our interpretation of water-column stratification during both EH and HS1 comes from IFA-$\delta^{13}C$ of the three species (Fig. 3g–i). Planktic foraminiferal $\delta^{13}C$ is challenging to interpret due to multi-variate influences of changes in primary productivity, $\delta^{13}C$ of dissolved inorganic carbon (which may be impacted by riverine discharge) and other carbonate system parameters such as pCO_2-$\delta^{13}C$, $[CO_3]^{2-}$ and pH[40]. We contend that the similarity between surface ocean

and subsurface IFA-$\delta^{13}C_c$ distributions across multiple depth-stratified species indicates increased mixing in the upper water column relative to intervals where they are separate. IFA-$\delta^{13}C_c$ histograms for the three different taxa are far more separated during EH and HS1 intervals than the LH interval (Fig. 3g–i). This observation indicates that distinct $\delta^{13}C$ calcification conditions existed for the three depth-stratified species during HS1 and the EH.

Unlike freshwater-driven stratification during the EH, we hypothesize that the HS1 water column resembles a transient state without a barrier layer (Fig. 3c), observed today before monsoon onset[41]. The resulting thermally mediated shoaling of the pycnocline impedes the sourcing of nutrients to the photic zone from depth[9,42]. The TraCE21ka simulation shows weakened ISM rainfall during HS1 relative to the LH associated with relaxed ISM circulation, weakened winds and anomalously high SSS in the BoB (Extended Data Figs. 5 and 6). Whereas multi-proxy palaeomonsoon records indicate ISM weakening relative to the LGM (Fig. 2a,e–i), TraCE21ka indicates spatial heterogeneity in ISM precipitation evolution between HS1 and the LGM (Extended Data Fig. 7a–d), albeit with strong drying simulated over portions of the GBM and Irrawaddy drainage basins. Nevertheless, simulated salinification over the BoB is accompanied by ocean warming across the Indian Ocean, consistent with reconstructed SST at Site U1446 and SO188-KL342 (Extended Data Fig. 7c–d). We infer that widespread tropical surface-ocean warming, muted ocean–atmosphere circulation and reduced winds during HS1 triggered oligotrophic conditions in the BoB by restricting eddy pumping and energetic mixing required for nutrient delivery and sustenance of modern levels[39] of primary production (Fig. 4).

Palaeoconstraints on future ocean dynamics

We conclude that BoB primary production is mediated by the interplay between nutrients, runoff, ocean warming and winds, bearing a non-linear relationship with ISM variability. To contextualize our findings alongside simulated changes under future greenhouse warming, we constructed temperature–salinity isopycnals for the BoB surface–ocean across palaeo, modern and future states (Fig. 4). We observe a pattern wherein a distinct range of isopycnals bounds intervals of moderate to high production. In contrast, EH and HS1 values—intervals when productivity was stifled according to our biogeochemical records—lie outside of this range. Alarmingly, we find that ensemble-mean CMIP6 values ($n = 34$ models) for both 'middle-of-the-line' and 'high-emissions' scenarios fall under a lowered isopycnal state (squares in Fig. 4), overlapping EH values. Unlike the EH, however, future intensification of ISM runoff is projected to occur without a significantly strengthened wind regime[5], which, alongside SST warming (as observed across the HS1 interval in the U1446 record), starkly increases the propensity of sustained upper-ocean stratification in the BoB (Fig. 3). In the context of the close relationship between density-driven stratification and primary production, our findings provide more clarity towards ambiguous results between CMIP5/CMIP6 climate projections and Earth-system model predictions and ultimately point towards future deterioration of BoB productivity under monsoon intensification driven by global change.

Online content

Any methods, additional references, Nature Portfolio reporting summaries, source data, extended data, supplementary information, acknowledgements, peer review information; details of author contributions and competing interests; and statements of data and code availability are available at https://doi.org/10.1038/s41561-025-01684-6.

References

1. Hossain, M. S., Sarker, S., Sharifuzzaman, S. M. & Chowdhury, S. R. Primary productivity connects hilsa fishery in the Bay of Bengal. *Sci. Rep.* **10**, 5659 (2020).
2. Lam, V. W. Y. & Pauly, D. Status of fisheries in 13 Asian large marine ecosystems. *Deep Sea Res. Part II* **163**, 57–64 (2019).
3. *State of World Fisheries and Aquaculture: Sustainability in Action* (FAO, 2020).
4. Sooraj, K. P., Terray, P. & Mujumdar, M. Global warming and the weakening of the Asian summer monsoon circulation: assessments from the CMIP5 models. *Clim. Dyn.* **45**, 233–252 (2015).
5. Katzenberger, A., Schewe, J., Pongratz, J. & Levermann, A. Robust increase of Indian monsoon rainfall and its variability under future warming in CMIP6 models. *Earth Syst. Dyn.* **12**, 367–386 (2021).
6. Kwiatkowski, L. et al. Twenty-first century ocean warming, acidification, deoxygenation, and upper-ocean nutrient and primary production decline from CMIP6 model projections. *Biogeosciences* **17**, 3439–3470 (2020).
7. Bopp, L. et al. Multiple stressors of ocean ecosystems in the 21st century: projections with CMIP5 models. *Biogeosciences* **10**, 6225–6245 (2013).
8. Prasanna Kumar, S. et al. Are eddies nature's trigger to enhance biological productivity in the Bay of Bengal. *Geophys. Res. Lett.* **31** (2004).
9. Narvekar, J. & Kumar, S. P. Seasonal variability of the mixed layer in the central Bay of Bengal and associated changes in nutrients and chlorophyll. *Deep Sea Res. Part I* **53**, 820–835 (2006).
10. Singh, A., Gandhi, N., Ramesh, R. & Prakash, S. Role of cyclonic eddy in enhancing primary and new production in the Bay of Bengal. *J. Sea Res.* **97**, 5–13 (2013).
11. Vinayachandran, P. N. Observations of barrier layer formation in the Bay of Bengal during summer monsoon. *J. Geophys. Res.* **107**, 8018–8019 (2002).
12. Singh, A., Jani, R. A. & Ramesh, R. Spatiotemporal variations of the $\delta^{18}O$–salinity relation in the northern Indian Ocean. *Deep Sea Res. Part I* **57**, 1422–1431 (2010).
13. Clemens, S. C., Kuhnt, W., LeVay, L. J. & Scientists, I. O. D. P. E. *International Ocean Discovery Program Expedition 353 Preliminary Report: Indian Monsoon Rainfall* (International Ocean Discovery Program, 2015).
14. Thirumalai, K. & Clemens, S. Monsoon reconstructions using bulk and individual foraminiferal analyses in marine sediments offshore India. *Curr. Sci.* **119**, 328–334 (2020).
15. Clemens, S. C. et al. Remote and local drivers of Pleistocene South Asian summer monsoon precipitation: a test for future predictions. *Sci. Adv.* **7**, eabg3848 (2021).
16. Guptha, M. V. S., Curry, W. B., Ittekkot, V. & Muralinath, A. S. Seasonal variation in the flux of planktic Foraminifera; sediment trap results from the Bay of Bengal, northern Indian Ocean. *J. Foraminifer. Res.* **27**, 5–19 (1997).
17. Thirumalai, K., Quinn, T. M. & Marino, G. Constraining past seawater $\delta^{18}O$ and temperature records developed from foraminiferal geochemistry. *Paleoceanogr. Paleoclimatol.* **31**, 1409–1422 (2016).
18. Gray, W. R. & Evans, D. Nonthermal influences on Mg/Ca in planktonic foraminifera: a review of culture studies and application to the Last Glacial Maximum. *Paleoceanogr. Paleoclimatol.* **34**, 306–315 (2019).
19. Ripperger, S., Schiebel, R., Rehkämper, M. & Halliday, A. N. Cd/Ca ratios of in situ collected planktonic foraminiferal tests. *Paleoceanography* https://doi.org/10.1029/2007PA001524 (2008).
20. Boyle, E. A., Labeyrie, L. D. & Duplessly, J.-C. Calcitic foraminiferal data confirmed by cadmium in aragonitic Hoeglundina: application to the Last Glacial Maximum in the northern Indian Ocean. *Paleoceanography* **10**, 881–900 (1995).
21. Lear, C. H. et al. Breathing more deeply: deep ocean carbon storage during the mid-Pleistocene climate transition. *Geology* **44**, 1035–1038 (2016).

22. Jaccard, S. L. et al. Subarctic Pacific evidence for a glacial deepening of the oceanic respired carbon pool. *Earth Planet. Sci. Lett.* **277**, 156–165 (2009).
23. Pattan, J. N. et al. Coupling between suboxic condition in sediments of the western Bay of Bengal and southwest monsoon intensification: a geochemical study. *Chem. Geol.* **343**, 55–66 (2013).
24. Lakhani, K. Q., Lynch-Stieglitz, J. & Monteagudo, M. M. Constraining calcification habitat using oxygen isotope measurements in tropical planktonic foraminiferal tests from surface sediments. *Mar. Micropaleontol.* **170**, 102074 (2022).
25. Behara, A. & Vinayachandran, P. N. An OGCM study of the impact of rain and river water forcing on the Bay of Bengal. *J. Geophys. Res. C* **121**, 2425–2446 (2016).
26. Liu, Z. et al. Transient simulation of last deglaciation with a new mechanism for Bolling-Allerod warming. *Science* **325**, 310–314 (2009).
27. Kudrass, H. R., Hofmann, A., Doose, H., Emeis, K.-C. & Erlenkeuser, H. Modulation and amplification of climatic changes in the Northern Hemisphere by the Indian summer monsoon during the past 80 k.y. *Geology* **29**, 63–65 (2001).
28. Zorzi, C. et al. When eastern India oscillated between desert versus savannah-dominated vegetation. *Geophys. Res. Lett.* **49**, e2022GL099417 (2022).
29. Saraswat, R., Lea, D. W., Nigam, R., Mackensen, A. & Naik, D. K. Deglaciation in the tropical Indian Ocean driven by interplay between the regional monsoon and global teleconnections. *Earth Planet. Sci. Lett.* **375**, 166–175 (2013).
30. Kumar, P. K. & Ramesh, R. Revisiting reconstructed Indian monsoon rainfall variations during the last ~25ka from planktonic foraminiferal $\delta^{18}O$ from the Eastern Arabian Sea. *Quat. Int.* **443**, 29–38 (2017).
31. Sijinkumar, A. V. et al. $\delta^{18}O$ and salinity variability from the Last Glacial Maximum to recent in the Bay of Bengal and Andaman Sea. *Quat. Sci. Rev.* **135**, 79–91 (2016).
32. Weldeab, S. et al. Impact of Indian Ocean surface temperature gradient reversals on the Indian summer monsoon. *Earth Planet. Sci. Lett.* **578**, 117327 (2022).
33. Phillips, S. C., Johnson, J. E., Giosan, L. & Rose, K. Monsoon-influenced variation in productivity and lithogenic sediment flux since 110 ka in the offshore Mahanadi Basin, northern Bay of Bengal. *Mar. Pet. Geol.* **58**, 502–525 (2014).
34. Zhou, X. et al. Dynamics of primary productivity in the northeastern Bay of Bengal over the last 26000 years. *Climate* **16**, 1969–1986 (2020).
35. Sijinkumar, A. V., Nath, B. N. & Clemens, S. North Atlantic climatic changes reflected in the Late Quaternary foraminiferal abundance record of the Andaman Sea, north-eastern Indian Ocean. *Palaeogeogr. Palaeoclimatol. Palaeoecol.* **446**, 11–18 (2016).
36. Ma, R. et al. North Indian Ocean circulation since the last deglaciation as inferred from new elemental ratio records for benthic foraminifera *Hoeglundina elegans*. *Paleoceanogr. Paleoclimatol.* **35**, e2019PA003801 (2020).
37. Sarma, V. V. S. S. et al. Effects of freshwater stratification on nutrients, dissolved oxygen, and phytoplankton in the Bay of Bengal. *Oceanography* **29**, 222–231 (2016).
38. Girishkumar, M. S., Ravichandran, M. & Pant, V. Observed chlorophyll-a bloom in the southern Bay of Bengal during winter 2006–2007. *Int. J. Remote Sens.* **33**, 1264–1275 (2012).
39. Mukherjee, A., Shankar, D., Chatterjee, A. & Vinayachandran, P. N. Numerical simulation of the observed near-surface East India Coastal Current on the continental slope. *Clim. Dyn.* **50**, 3949–3980 (2018).
40. Spero, H. J., Lerche, I. & Williams, D. F. Opening the carbon isotope 'vital effect' black box, 2, quantitative model for interpreting foraminiferal carbon isotope data. *Paleoceanography* **6**, 639–655 (1991).
41. Shroyer, E. et al. Bay of Bengal intraseasonal oscillations and the 2018 monsoon onset. *Bull. Am. Meteorolog. Soc.* **102**, E1936–E1951 (2018).
42. Madhu, N. V. et al. Lack of seasonality in phytoplankton standing stock (chlorophyll a) and production in the western Bay of Bengal. *Cont. Shelf Res.* **26**, 1868–1883 (2006).
43. Gray, W. R. et al. The effects of temperature, salinity, and the carbonate system on Mg/Ca in *Globigerinoides ruber* (white): a global sediment trap calibration. *Earth Planet. Sci. Lett.* **482**, 607–620 (2018).
44. Lambeck, K., Rouby, H., Purcell, A., Sun, Y. & Sambridge, M. Sea level and global ice volumes from the Last Glacial Maximum to the Holocene. *Proc. Natl Acad. Sci. USA* **111**, 15296–15303 (2014).
45. Dutt, S. et al. Abrupt changes in Indian summer monsoon strength during 33,800 to 5500 years BP. *Geophys. Res. Lett.* **42**, 5526–5532 (2015).
46. Schneider, U. et al. GPCC's new land surface precipitation climatology based on quality-controlled in situ data and its role in quantifying the global water cycle. *Theor. Appl. Climatol.* **115**, 15–40 (2013).
47. Balmaseda, M. A., Mogensen, K. & Weaver, A. T. Evaluation of the ECMWF ocean reanalysis system ORAS4. *Q. J. R. Meteorol. Soc.* **139**, 1132–1161 (2012).
48. Contreras-Rosales, L. A. et al. Evolution of the Indian Summer Monsoon and terrestrial vegetation in the Bengal region during the past 18 ka. *Quat. Sci. Rev.* **102**, 133–148 (2014).

Methods

Oceanographic setting

Nearly 3,000 km^3 of riverine freshwater fluxes annually into the BoB, making it one of the freshest oceanic basins[49,50]. Over 80% of this volume results from the runoff of summer monsoon precipitation sourced from adjacent continental regions[51], including discharge from the prominent Ganges–Brahmaputra–Meghna (GBM) river complex, which peaks during August and September[50,52], as a result of the ISM. Consequently, the northern BoB experiences SSS minima in the post-monsoon season during October and November (Fig. 1). Autumnal strengthening of northeasterly winds additionally facilitates the equatorward flow of the East India Coastal Current[39,51] (EICC). Accordingly, mean salinity and its variability in the EICC region (Fig. 1) are shaped by the intensity of ISM runoff[13–15,52–54].

Isotope mass balance and monsoon hydrology

IODP Site U1446 (19.08° N, 85.73° E; 1,430 m water depth; ~70 km offshore) is located in the Mahanadi Basin[13], within the core of the EICC flow path (Fig. 1). We infer past ISM intensity by reconstructing the stable oxygen isotope composition of surface-ocean waters ($\delta^{18}O_{sw}$; reported relative to VSMOW) at this site[55,56]. Changes in the isotopic composition of fluvial freshwater influx or that of direct precipitation over the BoB generates negligible change in $\delta^{18}O_{sw}$ at our site[15] (below). GBM riverine $\delta^{18}O$ has been shown to be decoupled from rainwater $\delta^{18}O_w$, and seasonal and interannual variability in GBM riverine $\delta^{18}O$ (~1 ‰ VSMOW) is muted relative to rainfall $\delta^{18}O$ variability (~8‰ VSMOW) (ref. 57). Rather, owing to the southwestward post-monsoon flow of the EICC, the volume of seasonal GBM discharge rather than its isotopic composition modulates $\delta^{18}O_{sw}$ variability at Site U1446 (refs. 12–15).

Clemens et al.[15] showed that runoff volume at the mouth of the Ganges, which has an average isotopic composition of −6‰, would have to change by only ~20% to alter the EICC $\delta^{18}O_{sw}$ composition by ~1‰ (equivalent to the reconstructed range of the $\delta^{18}O^*_{sw}$ difference between the early Holocene and the Heinrich Event in our record), corresponding to an ~50% decrease in seasonality at our site (Extended Data Fig. 2). On the other hand, the $\delta^{18}O$ of runoff would have to change by ~5.5‰ (that is, move from −6 to −11.5‰) to alter the EICC $\delta^{18}O_{sw}$ by ~1‰ for a constant volume of GBM outflow feeding into the EICC[15]. Using isotope-enabled simulations, Pausata et al. (2011) suggested[58] that the maximum Last Glacial Maximum (LGM) to Heinrich Stadial 1 (HS1) change in rainfall $\delta^{18}O$ is ~2–2.5‰; similarly Tharammal et al. suggested that early Holocene rainfall $\delta^{18}O$ is ~2‰ less than modern values in the core monsoon zone[59]. If we assume that average rainfall $\delta^{18}O$ over the GBM drainage area (1.08 × 106 km²) is −11 ‰ (including snowfall and snowmelt contributions[60]) at maximal values of 3 m per year across the entire basin, and that riverine $\delta^{18}O$ is −6‰ discharging 3,000 km^3 per year (ref. 50), then a rainwater isotopic anomaly of 3‰ over the entire drainage basin[58,59] would only change the deltaic values by about ~1‰ —a value far less than the 5.5‰ required to alter seawater ä^{18}O at Site U1446 by 1‰. Such a scenario of $\delta^{18}O_{sw}$ changes (independent of runoff change) is physically unlikely for EICC waters and would necessitate that deltaic waters running off into the BoB approach isotopic compositions similar to headwaters above 2,000-m elevation, which today[57] range from −11 to −16‰.

We quantify the relationship between ISM intensity and $\delta^{18}O_{sw}$ seasonality at our site using GBM runoff as input into a theoretical $\delta^{18}O_{sw}$ model and by using an EICC-specific salinity–$\delta^{18}O_{sw}$ relationship (Extended Data Fig. 1). Reanalysis data additionally affirm that post-monsoon outflow during October drives mean-annual $\delta^{18}O_{sw}$ values and their seasonal range—enabling us to estimate past seasonality from reconstructed mean-annual $\delta^{18}O_{sw}$ (regressions in Extended Data Fig. 2). We assume that $\delta^{18}O_{sw}$ seasonality of ~1.4 ‰ (VSMOW) at Site U1446 corresponds to peak ISM runoff of ~220 mm per month in the GBM catchment[61], amounting to ~8×10^4 m^3 s^{-1} of discharge flux[50].

To support this inference, we estimated the seasonal range and variability of GBM outflow by obtaining surface runoff in the GBM drainage area (18–29° N, 80–99.5° E) from the ERA-5 reanalysis dataset[62] and applied it to the following Rayleigh-derived equation[63], which describes the stable isotopic evolution of a watermass from a freshwater endmember:

$$\delta = \delta_i f^{\rho} + \frac{(1 - f^{\rho})(\beta\delta_{fw} - \varepsilon)}{\alpha + \beta + 1}$$

where, δ is the isotopic composition (in δ notation expressed in ‰ VSMOW) of an oceanic watermass (with an initial isotopic composition of δ_i), δ_{fw} is the isotopic composition of the freshwater endmember, α is the effective fractionation factor including kinetic effects, β is the change in runoff, ε is the oxygen isotope fractionation between vapour and liquid in ‰, f is the fraction of water left relative to the inital amount and $\rho = \frac{\alpha}{1-\beta} - 1$. We used $\alpha = 0.9902$, $\varepsilon = -9.8$ and assumed an initial isotopic composition of −6.09‰ based on observations[64] and used ERA-5 runoff values as input for β. Subsequently, we extracted the annual cycle from calculated $\delta^{18}O_{sw}$ (triangles in Extended Data Fig. 1) and compared it with available measurements of $\delta^{18}O_{sw}$ proximal to the Mahanadi Basin (stars in Extended Data Fig. 1) and SSS-derived $\delta^{18}O_{sw}$ values using an EICC-specific relationship[12,14]: $\delta^{18}O_{sw} = 0.36 \times S - 11.7$, where S is salinity. SSS was extracted from the ORA-S4 dataset[47] (1958–2013; 18.5–19.5° N, 85.5–86.5° E) and the interannual standard deviation for each month was ascribed as the uncertainty in the climatology (envelopes in Extended Data Fig. 1). We estimate that peak monsoon outflow from the GBM induces a $\delta^{18}O_{sw}$ range of 1.27 ± 0.40‰ (VSMOW). This is consistent with available (yet sparse and short-term) measurements[12] of $\delta^{18}O_{sw}$ proximal to the Mahanadi Basin (1.76 ± 0.57‰ VSMOW) and is in line with estimates from applying an EICC-specific[12,14,15] salinity–$\delta^{18}O_{sw}$ relationship to reanalysis SSS at our site (1.40 ± 0.47‰ VSMOW; Extended Data Fig. 1).

Additionally, we regressed mean-annual SSS-derived $\delta^{18}O_{sw}$ at Site U1446 along with October values (Extended Data Fig. 2a) and the seasonal range of each year (Extended Data Fig. 1b) using a bivariate approach[65]. We find strong covariability of mean-annual $\delta^{18}O_{sw}$ with both October minima ($r = 0.83$; $P < 0.01$) and the overall seasonal range ($r = 0.59$; $P < 0.01$), thereby confirming that post-monsoon October outflow modulates both the seasonal range and mean-annual $\delta^{18}O_{sw}$ at Site U1446 (Extended Data Fig. 2). We use this empirical relationship to estimate changes (%) in past seasonality relative to late Holocene values. Considering that some studies have inferred more substantial winter monsoon precipitation during glacial periods[30,66], any increase in salinity at Site U1446 due to winter monsoon weakening over the deglaciation would mask putative reductions due to ISM runoff strengthening and thus render our ISM change estimates as minimum estimates.

Site U1446 age model

IODP Site U1446 was drilled as part of Expedition 353 (‘*iMonsoon*’) in the northwestern BoB, located in the Mahanadi Basin (Fig. 1). Situated on a northwest–southeast trending ridge, the site is protected from deposition of turbidites; details about the sedimentological setting of the site are published elsewhere[13,15]. We built an age model on the upper ~7 m used for this study with 14 radiocarbon measurements (Extended Data Fig. 3) using Accelerator Mass Spectrometry on upper-ocean planktic foraminifera primarily including *Globigerinoides ruber*, *Trilobatus sacculifer*, *Globigerinoides conglobatus* and *Globigerinella siphonifera*. The radiocarbon dates were calibrated into calendar years before 1950 using the R code BACON[67] by applying the Marine13 calibration curve[68] and a local reservoir correction[69]. Observations of live benthic foraminifera (confirmed via Rose Bengal[13]) in the uppermost sediments are consistent with post-bomb radiocarbon values and confirm a modern age for the core top at Site U1446. Our radiocarbon age model reaffirms the expanded nature of the Holocene section of Site U1446

sediments, containing apparent sedimentation rates ~28–30 cm kyr^{-1} (more than sufficient for centennial-scale sampling), which decrease to 12.5–13.5 cm kyr^{-1} during the deglaciation (Extended Data Fig. 3). A version of the age–depth model used here has been previously published[28].

Paired Mg/Ca-$\delta^{18}O$ planktic foraminiferal geochemistry

We picked approximately 70–90 tests of planktic foraminifer *Globigerinoides ruber* (white variety; mainly of the *sensu stricto* morphotype variety) from the 250–350 µm size fraction in each sediment sample for paired stable isotope and trace elemental analysis. Tests were gently crushed and homogenized before being split for isotopic and elemental analysis. We measured the stable carbon ($\delta^{13}C_c$) and oxygen isotope composition ($\delta^{18}O_c$) of the calcite tests using a Kiel III Carbonate Device coupled to a Thermo Finnigan MAT 252 Isotope Ratio Mass Spectrometer (IRMS) housed at Brown University. Both $\delta^{18}O_c$ and $\delta^{13}C_c$ values are reported in per mille (‰) relative to the Vienna Pee Dee Belemnite scale (VPDB). In total, we measured 277 *G. ruber* samples along with 60 measurements of standards (Brown Yule Marble and Carrara). Repeated analyses ($n = 28$) of Brown Yule Marble yielded −2.26 ± 0.02 (1σ) ‰ for $\delta^{13}C_c$ and −6.46 ± 0.07‰ for $\delta^{18}O_c$, whereas repeated analyses ($n = 32$) of Carrara yielded 2.05 ± 0.02‰ and −1.89 ± 0.05‰, respectively.

Trace elemental ratios in *G. ruber* tests (250–350 µm size fraction), including Mg/Ca, U/Ca and Cd/Ca, were measured on an Element XR Sector Field Inductively Coupled Plasma Mass Spectrometer at Rutgers University. For the 'time-slice' intervals targeted for individual foraminiferal analysis (below and Table 1), Mg/Ca analysis was performed on a Thermo iCap 7000 Inductively Coupled Optical Emission Spectrophotometer (ICP-OES) housed at the University of Arizona Paleo² Lab[70]. Before analysis, samples were thoroughly processed for clay removal, with the application of both reductive and oxidative cleaning steps[71,72]. Despite rigorous cleaning protocols, we note that our inference for U/Ca is based on post-depositional incorporation (in contrast to the in situ inference of Cd/Ca and Mg/Ca) where elevated export of organic matter fluxes to sediments can cause increases in sedimentary U (our interpretation follows that of Lear et al., 2016). Support for such an interpretation comes from the magnitude of the elemental ratios, where Cd/Ca[19] and Mg/Ca[15] are consistent with upper-ocean incorporation, whereas that of U/Ca is consistent with sedimentary incorporation[21,22]. Elemental ratios were calculated from a calibration composed of varying concentrations of matrix-matched synthetic standards[73]. Reproducibility (1σ) was determined by repeated inductively coupled plasma mass spectrometer analyses of synthetic carbonate standards and was found to be better than 1.8% for Mg/Ca and 6% for Cd/Ca and U/Ca (note that error envelope for the multi-centennial Cd/Ca & U/Ca record in Fig. 2c is ~3% due to smoothing). Reproducibility (1σ) for the ICP-OES Mg/Ca measurements was 0.02 mmol mol^{-1} (relative standard deviation better than 0.5%), determined by repeat analyses of the ECRM carbonate standard. Elemental values of contaminants (Al/Ca and Fe/Ca) were routinely monitored, and samples with high Al/Ca (≥ 300 µmol mol^{-1}) and Fe/Ca (≥ 10 µmol mol^{-1}) were omitted. We found no correlation between Mn/Ca and U/Ca or Cd/Ca.

To investigate vertical stratification using depth-stratified planktic foraminifera during the intervals where individual foraminiferal analysis (IFA) was applied (that is, core top, early Holocene and Heinrich Stadial 1), we measured Mg/Ca ratios in 60–90 crushed tests of *G. ruber, T. sacculifer* and *N. dutertrei*. These individuals were picked from the 400–500-µm size fraction to mirror the IFA measurements, cleaned using oxidative steps[72] and measured using ICP-OES at the University of Arizona[70].

Individual foraminiferal stable isotope analyses

IFA[74] were performed on *G. ruber*, *T. sacculifer* and *N. dutertrei* specimens from the 400–500-µm size fraction. A one-year sediment trap study[16] in the northern BoB indicates that both *G. ruber* (W) and *T. sacculifer* occur throughout the year with minor, erratic pulses of abundance not tied to any season. Accordingly, variability in their IFA-$\delta^{18}O_c$ and -$\delta^{13}C_c$ probably reflects oceanographic conditions sampled throughout the year[14,75]. Though *N. dutertrei* abundances exhibit winter and summer peaks, Guptha et al.[16] found low but steady background fluxes throughout the year. Moreover, minor seasonal variability in expected foraminiferal $\delta^{18}O_c$ for subsurface depths (30–60 m) at our site coincides with the *N. dutertrei* calcification habitat; this supports the inference that IFA from this species samples the year-round range of conditions at depth. On the basis of comparisons with calculated $\delta^{18}O_c$ forward modelled from World Ocean Atlas temperature and salinity profiles (Extended Data Fig. 4), we estimate calcification depths[24] for these species to be ~10–30 m, ~15–45 m and ~40–60 m, respectively.

In total, we performed 548 stable oxygen and carbon isotope IFA measurements across three time periods (Fig. 3): the late Holocene (samples spanning from 0.7–0 ka; $n_{ruber} = 48$; $n_{sacculifer} = 75$; $n_{dutertrei} = 98$), the early Holocene (10–9.1 ka; $n_{ruber} = 47$; $n_{sacculifer} = 60$; $n_{dutertrei} = 58$) and Heinrich Stadial 1 (~ 17–16 ka; $n_{ruber} = 40$; $n_{sacculifer} = 59$; $n_{dutertrei} = 63$). IFA-$\delta^{18}O_c$ was measured on a Kiel IV Carbonate Device coupled to a Thermo Scientific MAT 253 + IRMS housed at the University of Arizona Paleo² Laboratory[76,77] and on the IRMS set-up at Brown University detailed above. Repeated multi-standard analyses displayed no mean offsets between the two laboratories. Samples ranged in mass from ~15–80 µg and no pressure correction was required nor applied for this range. Replicate standard analyses ($n = 129$) at the low-mass ranges indicated analytical precision better than 0.06‰ VPDB (1σ) for $\delta^{13}C_c$ and 0.08‰ VPDB for $\delta^{18}O_c$. A summary of values is provided in Table 1. To account for different numbers of IFA for different species across intervals, we used a Monte Carlo resampling approach to perform 1,000 paired *t*-tests. The only statistically significant $\delta^{18}O_c$ mean difference (paired *t*-test passed for all 1,000 Monte Carlo subselections at the $\alpha = 0.01$ level) between *G. ruber* and *T. sacculifer* arises for the HS1 period, whereas *N. dutertrei* mean $\delta^{18}O_c$ values are significantly different from the other species across all intervals (Table 1). Mean values of each species' IFA-$\delta^{13}C_c$ distributions are significantly different from each other across all intervals, with median separation larger during the EH and HS1 intervals. We also note that the core-top IFA $\delta^{13}C_c$ and $\delta^{18}O_c$ ranges obtained on all three species (>1.5‰) show values consistent with observations (Extended Data Fig. 4), showing that IFA on these species effectively samples seasonality and snapshots of year-round oceanic conditions.

During the EH, IFA-$\delta^{18}O_c$ overlaps the entire modern distribution but contains a thick 'fresh' tail that exceeds the lowest modern values by ~1–1.2‰ (VPDB). $\delta^{18}O_{sw}$ is the major control on this tail because mean temperature values (derived from multi-specimen Mg/Ca) for this period are only ~1 °C warmer than modern temperatures (amounting to ~0.22‰ in $\delta^{18}O_c$). Even if summers were warmer by ~2 °C (unlikely given the modern relationship between largely invariant summer SSTs and annual mean SST in this region[14]), this would explain only ~0.45‰ of the thicker early Holocene tail, leaving a full 0.75‰ in the IFA-$\delta^{18}O_c$ distribution to be explained by changes in $\delta^{18}O_{sw}$. This amounts to an ~45% increase in overall seasonality and is consistent with the ≥ 30% estimate from mean $\delta^{18}O^*_{sw}$ (Extended Data Fig. 2). IFA-$\delta^{13}C_c$ during the EH shows more marked separation between the median values of the three species compared to the LH interval. On the other hand, during HS1, we observe distinctly different means between both IFA-$\delta^{18}O_c$ and IFA-$\delta^{13}C_c$ across the three different depth-stratified species. This occurs at higher mean $\delta^{18}O_c$ values relative to the Holocene distributions and is, therefore, more sensitive to changes in temperature as opposed to freshwater influx[14]. The IFA distribution and ranges of values preclude that the calcification of any of the three species was restricted to any specific season during any of the investigated intervals.

Reconstructing temperature, $\delta^{18}O_{sw}$ and associated uncertainty

We infer past variations in mean annual, surface-ocean $\delta^{18}O_{sw}$ from the paired $\delta^{18}O_c$-Mg/Ca measurements on *G. ruber*. This species calcifies

in the upper ~30 m of the water column and is known to occur year round in the Bay of Bengal[16]. Thus, its $\delta^{18}O_c$ varies as a function of mean-annual SST and surface-ocean $\delta^{18}O_{sw}$—which at Site U1446 reflects GBM runoff. On glacial–interglacial timescales, $\delta^{18}O_{sw}$ is impacted by changes in global oceanic $\delta^{18}O_{sw}$ due to effective fractionation driven by land-ice build-up and melting. This necessitates a correction for the reconstructed $\delta^{18}O_{sw}$ to focus on local hydrographic variability free from global $\delta^{18}O_{sw}$ changes arising from varying global ice volume (hereafter denoted as $\delta^{18}O^*_{sw}$). To compute $\delta^{18}O^*_{sw}$, we used the PSU Solver algorithm[55], which employs an iterative bootstrap Monte Carlo procedure to solve for calcification temperature and $\delta^{18}O^*_{sw}$ and their uncertainties simultaneously. Several recent studies[18,43,78,79] have identified non-thermal influences on planktic foraminiferal Mg/Ca. Here we use an updated calibration equation[43] as input into PSU Solver, which explicitly considers the influence of salinity and pH on Mg/Ca variations (based on observations proximal to our core site[80], we used pH = 8.17 for Site U1446; pH = 8.10 for SO188-KL342; pH = 8.14 for SK237-GC04). Towards computing $\delta^{18}O^*_{sw}$, we use a high-resolution LGM-to-present sea-level curve[44] and an equation relating $\delta^{18}O_c$ to $\delta^{18}O_{sw}$, and calcification temperature, based on culture experiments[81]. We utilized an EICC-specific $\delta^{18}O_{sw}$–salinity relationship for U1446 and SO188-KL342, whereas we used the Arabian Sea $\delta^{18}O_{sw}$–salinity relationship for the Malabar Coast[12]. We also updated the age model of SO188-KL342 by combining radiocarbon-derived ages from two different studies[32,48] and using two tie points to the Mawmluh Cave speleothem $\delta^{18}O$ record[45] at ~14 ka and ~16.2 ka. This age model was used to plot both leaf-wax δD and $\delta^{18}O^*_{sw}$ along with its uncertainty (Fig. 2).

We used the same framework of equations (based on Gray et al.[43] and Bemis et al.[81]) to estimate the temperature, $\delta^{18}O^*_{sw}$ and salinity values across the three species reported in Table 1 using PSU Solver. In general[82], ±1σ uncertainties in temperature, $\delta^{18}O^*_{sw}$ and salinity are approximately ~1.1 °C, −0.5‰ and 0.8‰, respectively, for the multi-test analyses (based on average uncertainties in the multi-test paired Mg/Ca-$\delta^{18}O$ *G. ruber* reconstruction). For the temperature–salinity diagram in Fig. 4, we used the inverted temperature and salinity values along with their 2σ uncertainty derived from the PSU Solver algorithm[55] for the stipulated time periods.

Abundance of *Globorotalia* as a palaeoproductivity indicator

To reconstruct the relative abundance of *Globorotalia* species, we counted specimens picked from the >63-µm fraction of dried U1446 sediment at the University of Arizona. We split these samples using a *Kreatvika* sample splitter and ensured that each assemblage had at least ~350–500 total specimens before calculating relative species abundances. Samples without the absolute abundance to provide sufficient total numbers of foraminifera were discarded. Across each sample, planktic foraminiferal tests were identified to the species level. Relative abundances were calculated based on the resultant counts. Overall, we summed the abundances of *Gr. menardii*, *Gr. ungulata*, *Gr. scitula* and *Gr. tumida* (listed in order of typical abundances) to compute the percentage of Globorotalids (Fig. 2d).

Five lines of evidence support our inference that *Globorotalia* abundances are tightly coupled to variations in the export production of particulate organic matter: (1) culturing studies demonstrate the strong dietary preference of *Globorotalia* spp. to feed on accumulations of particulate organic matter[83], (2) field studies have found that elevated barium concentrations[84] in *Globorotalia* tests are consistent[85] with a potential microhabitat of aggregated organic matter ('marine snow'), (3) core-top $\delta^{18}O_c$ values (−1.2‰) indicate apparent calcification depths[86] positioned close to the deep chlorophyll maxima (~80–100 m) in the northern BoB[9], (4) low carbon isotope values ($\delta^{13}C_c \leq 1$‰) of core-top *Globorotalia* tests are consistent with phytoplankton-derived sources and **(5)** although no *Globorotalia*-focused sediment trap study has been conducted on the Indian margin proximal to our site, the available evidence of seasonal *Globorotalia menardii* populations in 'open ocean' northern BoB sediment traps[16] show minimal-to-zero abundances during the post-monsoon season, when barrier-layer formation is most pronounced. January–March was the preferred season for peak *Gr. menardii* fluxes according to the one-year (November 1988–1989) sediment trap study[16] in the northern BoB. Several individuals persisted until June–August, after which they disappeared in September–October, when ISM runoff flows into the BoB and triggers barrier-layer formation. Accordingly, we expect lowered organic matter production to result in low-to-zero relative *Globorotalia* abundances in the U1446 record. On the other hand, increased relative abundance of *Globorotalia* could point towards an expanding seasonal niche into the post-monsoon season (that is, during times of lower year-round stratification) or towards more favourable conditions during January–August. We note, however, that a recent reconstruction of palaeoproductivity based on coccolith assemblages at a site proximal to the Irrawaddy outflow points to increasing productivity across HS1[34], thereby differing from the *Globorotalia* species abundances at Site U1446 in the northwest BoB and SK168 in the Andaman Sea. We suggest this disparity may arise from spatial variability reflecting different trends in primary productivity changes within the BoB, or via differences in carbonate versus organic matter production.

Analysis of the TraCE21ka transient simulation

We investigated climate model simulations of ISM variability over the deglaciation and during the early Holocene (EH), by evaluating output from the TraCE21ka transient simulation of the past 21,000 years[26]. This simulation was performed using the coupled general circulation model, the National Center for Atmospheric Research Community Climate System Model version 3 (NCAR CCSM3), the details of which are previously published[26]. We examined: (1) the evolution of core monsoon zone winds and ISM precipitation during June–September and sea surface salinity (SSS) during October over the past 21,000 years (Extended Data Fig. 5), (2) climate anomalies of Heinrich Stadial 1 (HS1; 17.5–16.5 ka) and the early Holocene (EH; 10.5–9.5 ka) relative to the late Holocene (LH; 1 ka) to facilitate model comparisons for our IFA time slices (Extended Data Fig. 6) and (3) HS1 and EH climate anomalies relative to the Last Glacial Maximum (21–20 ka) and the earliest Holocene (11.7–11.0 ka), that is, intervals just preceding HS1 and the EH, respectively, to investigate mechanisms of transient ISM changes (Extended Data Fig. 7).

The TraCE21ka simulation provides strong support that salinity variability in the EICC region and ISM precipitation is significantly anti-correlated over the past 21 ka (Extended Data Fig. 5b,c), in accordance with our inference of $\delta^{18}O^*_{sw}$ at Site U1446 serving as a record of ISM rainfall intensity over the core monsoon zone. The simulation also shows that the strongest surface winds (at 850 hPa) persisted during the EH (Extended Data Fig. 6g), alongside the highest ISM precipitation intensity and associated SSS minima (Extended Data Figs. 5 and 6g–i) over the past 21 ka—in agreement with multi-proxy palaeomonsoon reconstructions[32,48,87,88]. Additionally, the transient response of the ISM simulated by TraCE21ka from the earliest Holocene into the EH involved abrupt increases in precipitation across the ISM realm (Extended Data Fig. 7f), northern Indian Ocean freshening (Extended Data Fig. 7g) and minimal SST changes in the BoB, also in agreement with reconstructed palaeomonsoon runoff (Fig. 2). Relative to the LH, HS1 precipitation over the subcontinent is greatly reduced (Extended Data Fig. 6e), concurrent with positive surface salinity anomalies in the BoB (Extended Data Fig. 6f). Northeasterly surface wind anomalies persisted over the subcontinent during HS1 relative to the LH (Extended Data Fig. 6d) and signify greatly weakened ISM circulation. With respect to the LH period, the TraCE21ka simulation is consistent with multi-proxy palaeomonsoon reconstructions from the Indian Subcontinent and suggests that the EH was a time of peak monsoon intensity and that severely weakened ISM rainfall relative to modern intensity prevailed during HS1.

We observe some disparity in the transient response of the ISM during HS1 relative to the LGM as delineated by the TraCE21ka simulation versus the multi-proxy reconstructions. TraCE21ka simulates minimal change in surface winds and precipitation in the core monsoon zone between the LGM and HS1 (Extended Data Fig. 5); in contrast, multi-proxy reconstructions including records of marine $\delta^{18}O_{sw}$ and terrestrial leaf-wax δD and speleothem $\delta^{18}O$ all agree that ISM rainfall and circulation during HS1 was more subdued relative to the LGM (Fig. 2). Yet, TraCE21ka simulates widespread surface–ocean salinification in the BoB (Extended Data Fig. 7c) alongside weakened precipitation anomalies in the central and northern Indian Ocean but with a band of increased precipitation over the Indian Subcontinent (Extended Data Fig. 7b). Whereas TraCE21ka shows that the core monsoon zone encountered slightly increased HS1 precipitation relative to the LGM, positive SSS anomalies in the northern BoB are consistent with the advection of anomalously high-salinity waters from the central and northern Indian Ocean, and due to diminished runoff towards the northeastern BoB, including parts of the GBM and Irrawady drainage basins (Extended Data Fig. 7c). We suggest that more terrestrial palaeomonsoon records covering HS1 from peninsular India[89] will aid in informing whether this disparity between LGM and HS1 in TraCE21ka is truly inconsistent with palaeodata.

Analysis of CMIP6 simulations

To place CMIP6 simulations on the temperature–salinity diagram (Fig. 4), we calculated the annual mean values of sea surface temperature and salinity at the grid cell closest to the U1446 core site across a suite of models. We averaged 100 years for the pre-industrial (PI) control experiment and the years 2081–2100 for the other experiments (20 years). The years 2081–2100 were available for most simulations across the Shared Socioeconomic Pathways (SSP) scenarios SSP5–8.5 and SSP2–4.5, except for one model (IITM-ESM) where we used 19-year means from 2081 to 2099 instead. Values were calculated for 34 model simulations listed in Table Atlas.SM.2 of the Intergovernmental Panel on Climate Change (IPCC) 2021 report: ACCESS-CM2, ACCESS-ESM1-5, AWI-CM-1-1-MR, BCC-CSM2-MR, CanESM5, CESM2, CESM2-WACCM, CMCC-CM2-SR5, CNRM-CM6-1, CNRM-CM6-1-HR, CNRM-ESM2-1, EC-Earth3, EC-Earth3-Veg, EC-Earth3-Veg-LR, FGOALS-g3, GFDL-CM4, GFDL-ESM4, HadGEM3-GC31-LL, IITM-ESM, INM-CM4-8, INM-CM5-0, IPSL-CM6A-LR, KACE-1-0-G, KIOST-ESM, MIROC-ES2L, MIROC6, MPI-ESM1-2-HR, MPI-ESM1-2-LR, MRI-ESM2-0, NESM3, NorESM2-LM, NorESM2-MM, UKESM1-0-LL and FGOALS-f3-L. Calculations were performed on all models with sea surface temperature and salinity output accessible through Pangeo, which consisted of different subsets of the above: 34 models for the pre-industrial control, 33 models for SSP2–4.5 and 34 models for SSP5–8.5.

Data availability

All datasets produced in this study are available via Zenodo[90] at https://doi.org/10.5281/zenodo.14994416 (ref. 90). The map in Fig. 1 was generated using open-source Python software (Code availability statement).

Code availability

Open-sourced Python code was used to make the figures, perform the analyses and all calculations including the following modules and their required dependencies: matplotlib[91], pandas[92], NumPy[93], xarray[94], cartopy[95], SciPy[96], Pangeo, seaborn and seawater. All codes generated for this Article (including data) are available via GitHub at https://github.com/planktic/paleoISMthirumalai2025.

References

49. Sengupta, S., Parekh, A., Chakraborty, S., Ravi Kumar, K. & Bose, T. Vertical variation of oxygen isotope in Bay of Bengal and its relationships with water masses. *J. Geophys. Res. Oceans* **118**, 6411–6424 (2013).
50. Jian, J., Webster, P. J. & Hoyos, C. D. Large-scale controls on Ganges and Brahmaputra river discharge on intraseasonal and seasonal time-scales. *Q. J. R. Meteorol. Soc.* **135**, 353–370 (2009).
51. Shetye, S. R. et al. Hydrography and circulation in the western Bay of Bengal during the northeast monsoon. *J. Geophys. Res. Oceans* **101**, 14011–14025 (1996).
52. Durand, F., Papa, F., Rahman, A. & Bala, S. K. Impact of Ganges–Brahmaputra interannual discharge variations on Bay of Bengal salinity and temperature during 1992–1999 period. *J. Earth Syst. Sci.* **120**, 859–872 (2011).
53. Benshila, R. et al. The upper Bay of Bengal salinity structure in a high-resolution model. *Ocean Modell.* **74**, 36–52 (2014).
54. Dandapat, S., Gnanaseelan, C. & Parekh, A. Impact of excess and deficit river runoff on Bay of Bengal upper ocean characteristics using an ocean general circulation model. *Deep Sea Res. Part II* **172**, 104714 (2020).
55. Thirumalai, K. & Richey, J. N. Potential for paleosalinity reconstructions to provide information about AMOC variability. *US Clivar Var.* **14**, 8–12 (2016).
56. Thirumalai, K. Salty seas sway global glacial cycles. *Nature* **617**, 258–259 (2023).
57. Kumar, A., Sanyal, P. & Agrawal, S. Spatial distribution of $\delta^{18}O$ values of water in the Ganga river basin: insight into the hydrological processes. *J. Hydrol.* **571**, 225–234 (2019).
58. Pausata, F. S. R., Battisti, D. S., Nisancioglu, K. H. & Bitz, C. M. Chinese stalagmite $\delta^{18}O$ controlled by changes in the Indian monsoon during a simulated Heinrich event. *Nat. Geosci.* **4**, 474–480 (2011).
59. Tharammal, T. et al. Orbitally driven evolution of Asian monsoon and stable water isotope ratios during the Holocene: isotope-enabled climate model simulations and proxy data comparisons. *Quat. Sci. Rev.* **252**, 106743 (2021).
60. Dasgupta, B., Ajay, A., Kumar, A., Thamban, M. & Sanyal, P. Isoscape of surface runoff in high mountain catchments: an alternate model for meteoric water characterization and its implications. *J. Geophys. Res. Atmos.* **126**, e2020JD033950 (2021).
61. Mahto, S. S. & Mishra, V. Does ERA-5 outperform other reanalysis products for hydrologic applications in India. *J. Geophys. Res. Atmos.* **124**, 9423–9441 (2019).
62. Hersbach, H. et al. The ERA5 global reanalysis. *Q. J. R. Meteorol. Soc.* **146**, 1999–2049 (2020).
63. Singh, A., Mohiuddin, A., Ramesh, R. & Raghav, S. Estimating the loss of Himalayan glaciers under global warming using the $\delta^{18}O$–salinity relation in the Bay of Bengal. *Environ. Sci. Technol. Lett.* **1**, 249–253 (2014).
64. Lambs, L., Balakrishna, K., Brunet, F. & Probst, J. L. Oxygen and hydrogen isotopic composition of major Indian rivers: a first global assessment. *Hydrol. Process.* **19**, 3345–3355 (2005).
65. Thirumalai, K., Singh, A., Ramesh, R. & Ramesh, R. A MATLAB™ code to perform weighted linear regression with (correlated or uncorrelated) errors in bivariate data. *J. Geol. Soc. India* **77**, 377–380 (2011).
66. Sarkar, A., Ramesh, R., Bhattacharya, S. K. & Rajagopalan, G. Oxygen isotope evidence for a stronger winter monsoon current during the last glaciation. *Nature* **343**, 549–551 (1990).
67. Blaauw, M. & Christen, J. A. Flexible paleoclimate age–depth models using an autoregressive gamma process. *Bayesian Anal.* **6**, 457–474 (2011).
68. Reimer, P. J. et al. IntCal13 and Marine13 radiocarbon age calibration curves 0–50,000 years cal BP. *Radiocarbon* **55**, 1869–1887 (2013).

69. Raj, H., Bhushan, R., Muruganantham, M., Nambiar, R. & Dabhi, A. J. Marine reservoir age correction for the Andaman Basin. *Radiocarbon* **62**, 1339–1347 (2020).
70. Prabhakar, M. et al. Morphotypical and geochemical variations of planktic foraminiferal species in Siberian and central Arctic ocean core tops. *J. Foraminifer. Res.* **54**, 1–19 (2024).
71. Rosenthal, Y., Boyle, E. A. & Labeyrie, L. Last glacial maximum paleochemistry and deepwater circulation in the Southern Ocean: evidence from foraminiferal cadmium. *Paleoceanography* **12**, 787–796 (1997).
72. Barker, S., Greaves, M. & Elderfield, H. A study of cleaning procedures used for foraminiferal Mg/Ca paleothermometry. *Geochem. Geophys. Geosyst.* https://doi.org/10.1029/2003GC000559 (2003).
73. Rosenthal, Y., Field, M. P. & Sherrell, R. M. Precise determination of element/calcium ratios in calcareous samples using sector field inductively coupled plasma mass spectrometry. *Anal. Chem.* **71**, 3248–3253 (1999).
74. Fehrenbacher, J. S. et al. Individual foraminiferal analyses: a review of current and emerging geochemical techniques. *J. Foraminifer. Res.* **54**, 312–331 (2024).
75. Thirumalai, K., Partin, J. W., Jackson, C. S. & Quinn, T. M. Statistical constraints on El Niño Southern Oscillation reconstructions using individual foraminifera: a sensitivity analysis. *Paleoceanography* **28**, 401–412 (2013).
76. Thirumalai, K., Cohen, A. S. & Taylor, D. Hydrologic controls on individual ostracode stable isotopes in a desert lake: a modern baseline for Lake Turkana. *Geochem. Geophys. Geosyst.* **24**, e2022GC010790 (2023).
77. Jana, D., Torres, M., Evans, K., Jayan, A. K. & Thirumalai, K. Paired X-ray micro CT scanning and individual foraminifera isotopic analysis reveal (de)coupled changes in carbonate preservation and temperature. *Paleoceanogr. Paleoclimatol.* **39**, e2023PA004821 (2024).
78. Tierney, J. E., Malevich, S. B., Gray, W., Vetter, L. & Thirumalai, K. Bayesian calibration of the Mg/Ca paleothermometer in planktic foraminifera. *Paleoceanogr. Paleoclimatol.* **34**, 2005–2030 (2019).
79. Holland, S. M. The stratigraphy of mass extinctions and recoveries. *Annu. Rev. Earth Planet. Sci.* **48**, 75–97 (2020).
80. Sarma, V. V. S. S. et al. Elevated acidification rates due to deposition of atmospheric pollutants in the coastal Bay of Bengal. *Geophys. Res. Lett.* **48**, e2021GL095159 (2021).
81. Bemis, B. E., Spero, H. J., Bijma, J. & Lea, D. W. Reevaluation of the oxygen isotopic composition of planktonic foraminifera: experimental results and revised paleotemperature equations. *Paleoceanography* **13**, 150–160 (1998).
82. Mehta, S., Singh, A. & Thirumalai, K. Uncertainty in palaeosalinity estimates from foraminiferal geochemical records in the northern Indian Ocean. *Palaeogeogr. Palaeoclimatol. Palaeoecol.* **569**, 110326 (2021).
83. Spindler, M., Hemleben, C., Salomons, J. B. & Smit, L. P. Feeding behavior of some planktonic foraminifers in laboratory cultures. *J. Foraminifer. Res.* **14**, 237–249 (1984).
84. Lea, D. W. & Boyle, E. A. Barium in planktonic foraminifera. *Geochim. Cosmochim. Acta* **55**, 3321–3331 (1991).
85. Fehrenbacher, J. S. et al. Ba/Ca ratios in the non-spinose planktic foraminifer *Neogloboquadrina dutertrei*: evidence for an organic aggregate microhabitat. *Geochim. Cosmochim. Acta* **236**, 361–372 (2018).
86. Stainbank, S. et al. Controls on planktonic foraminifera apparent calcification depths for the northern equatorial Indian Ocean. *PLoS ONE* **14**, e0222299 (2019).
87. Marzin, C., Kallel, N., Kageyama, M., Duplessy, J.-C. & Braconnot, P. Glacial fluctuations of the Indian monsoon and their relationship with North Atlantic climate: new data and modelling experiments. *Climate* **9**, 2135–2151 (2013).
88. Goodbred, S. L. Jr & Kuehl, S. A. Enormous Ganges–Brahmaputra sediment discharge during strengthened early Holocene monsoon. *Geology* **28**, 1083–1086 (2000).
89. Ramya Bala, P. et al. Paleovegetation dynamics in an alternative stable states landscape in the montane Western Ghats, India. *Holocene* **32**, 297–307 (2021).
90. Thirumalai, K. Indian summer monsoon runoff variability, foraminiferal biogeochemical changes, and radiocarbon ages since the Last Glacial Maximum from Site U1446, NW Bay of Bengal. *Zenodo* https://doi.org/10.5281/zenodo.14994416 (2025).
91. Hunter, J. D. Matplotlib: a 2D graphics environment. *Comput. Sci. Eng.* **9**, 90–95 (2007).
92. McKinney, W. Data structures for statistical computing in Python. In *Proc. 9th Python in Science Conf*. 51–56 (SciPy, 2010).
93. Oliphant, T. *NumPy: A Guide to NumPy* (Continuum Press, 2006).
94. Hoyer, S. & J., H. xarray: N-D labeled arrays and datasets in Python. *J. Open Res. Softw.* **5** (2017).
95. Met, O. Cartopy: A Cartographic Python Library with a Matplotlib Interface. *Github* https://github.com/SciTools/cartopy (2015).
96. Jones, E., Oliphant, T. & Peterson, P. *SciPy: Open Source Scientific Tools for Python* (ScienceOpen, 2001).

Acknowledgements

We acknowledge support from the International Ocean Discovery Program (IODP) and are grateful to the IODP Expedition 353 scientific party and JOIDES Resolution staff that enabled successful core sample recovery. We thank M. Glicksman and M. Lis for their assistance in sample preparation. This work was supported by National Science Foundation grants AGS–2103077 and OCE–2423147 to K.T.

Author contributions

K.T., S.C.C. and Y.R. conceived the study and experimental design. K.T., S.C.C., Y.R., K.B., S.C., M.F. and L.V. generated measurements for the datasets presented in this Article. S.C.C., S.D., L.P.Z., and L.G. assisted K.T. in generating an age model for Site U1446. M.E., J.C., L.L. and Z.L. assisted K.T. in retrieving and interpreting the climate model output. A.S. and V.M. assisted K.T. in addressing productivity, ocean and monsoon dynamics in the Bay of Bengal. K.T. generated all the figures and wrote the paper with input from all authors. All authors interpreted the results and extensively revised the paper.

Competing interests

The authors declare no competing interests.

Additional information

Extended data is available for this paper at https://doi.org/10.1038/s41561-025-01684-6.

Correspondence and requests for materials should be addressed to K. Thirumalai.

Peer review information *Nature Geoscience* thanks Ajoy Bhaumik, Kelly Gibson and the other, anonymous, reviewer(s) for their contribution to the peer review of this work. Primary Handling Editor: James Super, in collaboration with the *Nature Geoscience* team.

https://doi.org/10.1038/s41561-025-01684-6

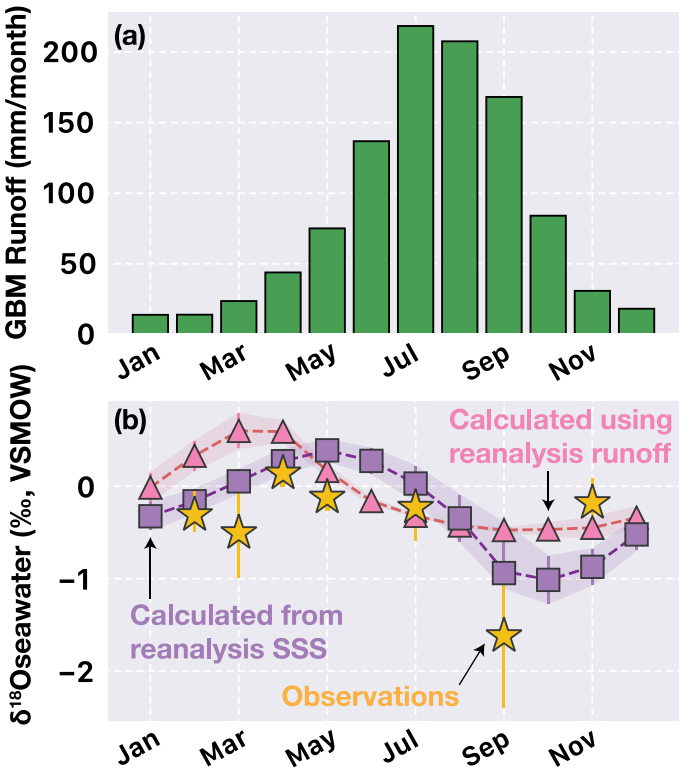

Extended Data Fig. 1 | Observed ISM Runoff and Site U1446 seawater $\delta^{18}O$ Seasonality. (a) Monthly-averaged ERA-5 runoff for the Ganges-Brahmaputra-Meghna (GBM) drainage basin (80–99.5°E, 18–29°N) and **(b)** observed[12] and calculated[17] $\delta^{18}O_{sw}$ at Site U1446, offshore Mahanadi Basin, northwestern Bay of Bengal. Observed $\delta^{18}O_{sw}$ (yellow stars) values were subsampled from a previous compilation[12] where the error bars represent the standard deviation of available measurements in that month (1σ whiskers based on a minimum of 5 observations; data unavailable for January, June, August, October, and December). SSS-derived $\delta^{18}O_{sw}$ (purple squares) values were calculated from ORA-S4 reanalysis salinity (n = 480 months) using an EICC-specific equation[14]. Seasonality in $\delta^{18}O_{sw}$ via GBM runoff (pink triangles) as input was calculated from a theoretical fractionation model (see Methods). Note that minima in $\delta^{18}O_{sw}$ occurs during September–to–October, lagging peak runoff values by ~1 month, and that available $\delta^{18}O_{sw}$ values in the EICC region during September are even lower than modeled values. All markers in the above plot depict median values as central measure.

https://doi.org/10.1038/s41561-025-01684-6

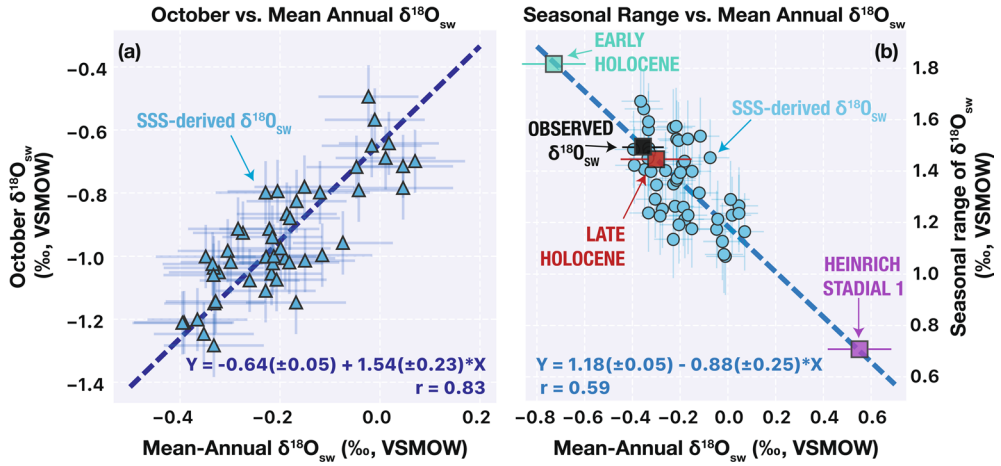

Extended Data Fig. 2 | Relationship between estimated mean-annual and October $\delta^{18}O_{sw}$, and the overall seasonal range at Site U1446. Scatterplot of SSS-derived mean-annual $\delta^{18}O_{sw}$ (using a region-specific equation on reanalysis SSS data[14]) with **(a)** October $\delta^{18}O_{sw}$ (blue triangles) and **(b)** its seasonal range (blue circles; maximum minus minimum values in a year) at Site U1446. Lines of best fit were built using (solely) the SSS-derived $\delta^{18}O_{sw}$ values on both plots (dashed blue lines), incorporating bivariate uncertainty in the parameters (slope, intercept, and correlation coefficients are provided at the bottom[65]), where 1σ errorbars are based on average error propagation for $\delta^{18}O_{sw}$ inversion (based on 225 downcore points), including analytical and sampling error[17]. The resultant covariability indicates that October $\delta^{18}O_{sw}$ minima drive yearly-averaged $\delta^{18}O_{sw}$ values, which are in turn, highly correlated with the seasonal range of $\delta^{18}O_{sw}$ at Site U1446; 1σ errorbars for the seasonal range were derived from bootstrap resampling (n = 480). This relationship thereby allows us to estimate past seasonality based on our mean-annual $\delta^{18}O_{sw}$ reconstruction. For (b) we also plot available observations of $\delta^{18}O_{sw}$ near the Mahanadi Basin (black square) and reconstructed $\delta^{18}O^{*}_{sw}$ for the late Holocene (red square), early Holocene (green square), and Heinrich Stadial 1 (purple square). Note that these reconstructed points of mean-annual $\delta^{18}O_{sw}$ are plotted *on* the line of best fit to estimate changes in seasonality during that interval. For example, our $\delta^{18}O_{sw}$ record indicates a value of ~0.55 ‰ (VSMOW) for HS1, which yields a seasonal range of ~0.7 ‰ (VSMOW) – a ~ 45% decrease relative to the late Holocene seasonal range of ~1.45 ‰.

https://doi.org/10.1038/s41561-025-01684-6

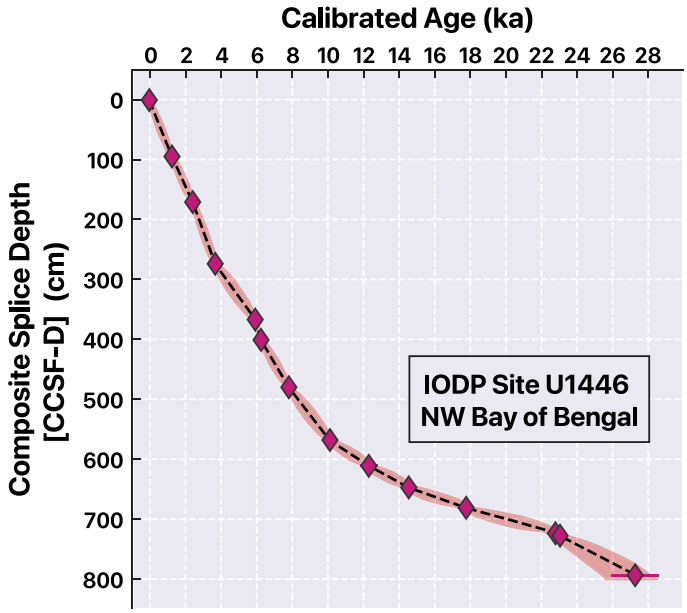

Extended Data Fig. 3 | Age model for upper 7 m of IODP Site U1446 splice used in this study. Posterior calibrated ages (diamonds are weighted-means) and uncertainty distributions (envelope) derived from age-modeling uncertainty software, BACON[67]. Analytical ^{14}C errors on individual ages are depicted using ±1σ uncertainty reported from AMS measurements (although most are smaller than the plotted symbols). Radiocarbon measurements were performed using samples containing pristine specimens of upper-ocean planktic foraminiferal species and corrected using the Marine13 curve with a marine reservoir age ΔR correction of ± 40 years[69].

https://doi.org/10.1038/s41561-025-01684-6

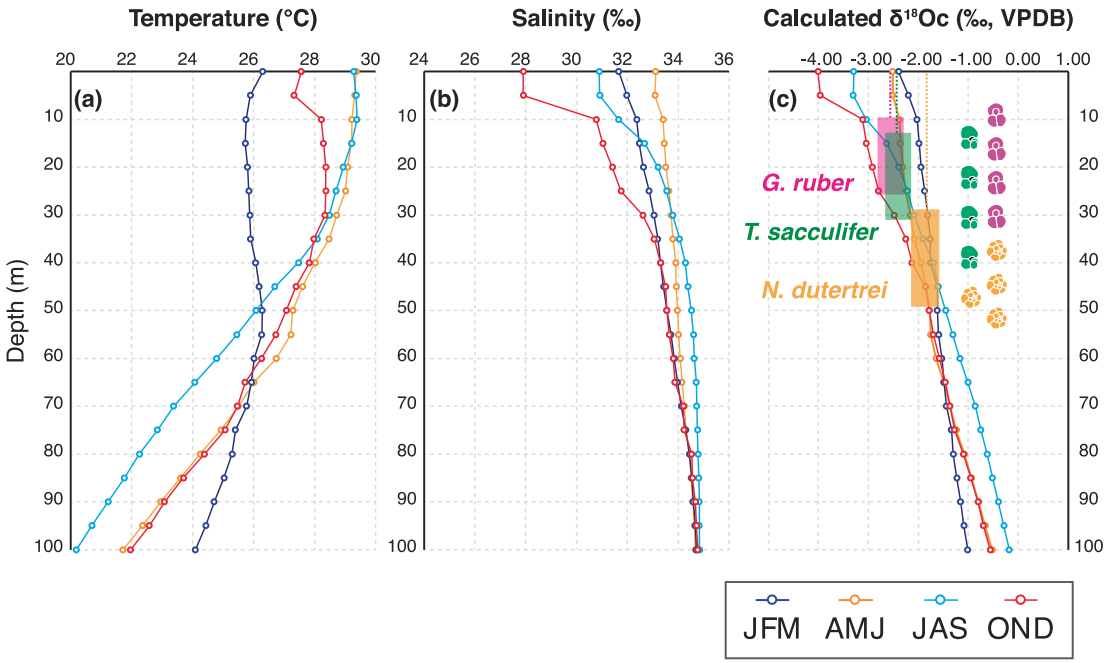

Extended Data Fig. 4 | Water column properties and foraminiferal calcification depth habitat at Site U1446. Average seasonal water column **(a)** temperature, **(b)** salinity, and **(c)** calculated $\delta^{18}O_c$ profiles at Site U1446 from the World Ocean Atlas Database, alongside median IFA-$\delta^{18}O_c$ for different species and their estimated depth of calcification ranges, based on the intersection of measured median $\delta^{18}O_c$ values and variability within the calculated $\delta^{18}O_c$ seasonal depth profile. $\delta^{18}O_c$ was calculated from temperature and salinity using the low-light equation[81], and local surface-ocean[14] and subsurface[49] $\delta^{18}O_{sw}$-salinity relationships for 0–40 m and 40–100 m respectively. JFM: January–March (winter); AMJ: April–June (pre-monsoon season); JAS: July–September (monsoon), OND: October–December (post-monsoon season).

https://doi.org/10.1038/s41561-025-01684-6

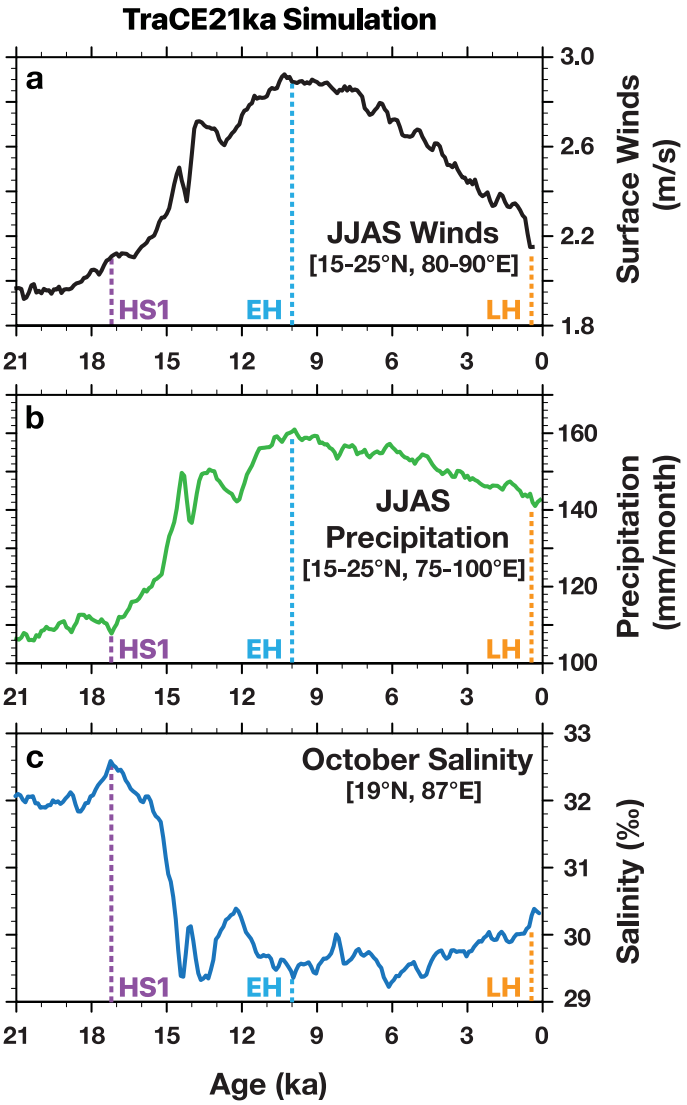

Extended Data Fig. 5 | TraCE21ka simulation output from 21ka to present. Surface winds **(a)** and precipitation **(b)** during June-July-August-September (JJAS) over the core monsoon zone of India, with October surface-ocean salinity **(c)** from the grid point most proximal to Site U1446. HS1 = Heinrich Stadial 1; EH = Early Holocene; LH = Late Holocene (corresponding to the IFA timeslices).

https://doi.org/10.1038/s41561-025-01684-6

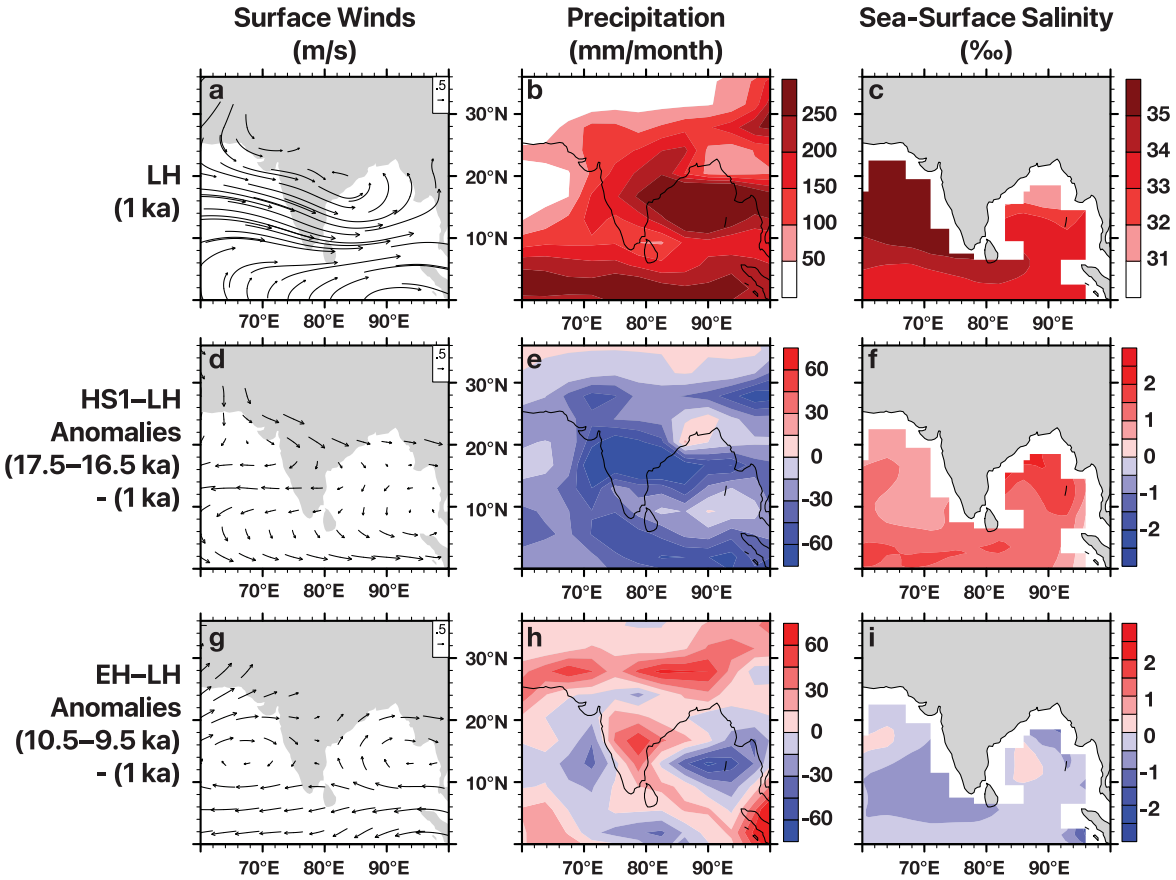

Extended Data Fig. 6 | TraCE21ka Late Holocene (LH) mean-state and anomalies relative to Heinrich Stadial 1 (HS1) and the early Holocene (EH). Mean June–September surface winds (**a**), and precipitation (**b**) and October sea-surface salinity (**c**) for the LH, alongside anomalies of these variables relative to HS1 (**d**–**f**), and the EH (**g**–**i**).

https://doi.org/10.1038/s41561-025-01684-6

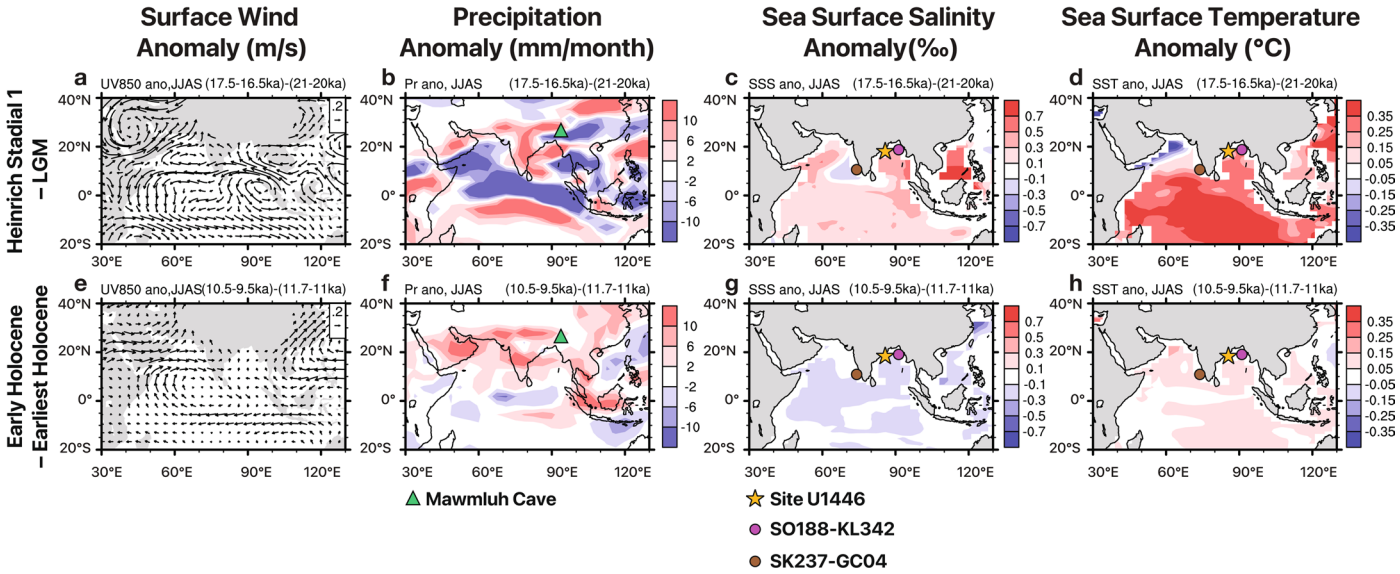

Extended Data Fig. 7 | Simulated climate anomalies for Heinrich Stadial 1 (HS1; 17.5–16.5 ka) and the early Holocene (EH; 10.5–9.5 ka) relative to the Last Glacial Maximum (21–20 ka) and the earliest Holocene (11.7–11.0 ka), respectively. Surface winds (**a, e**), precipitation (**b, f**), sea-surface salinity (**c, g**) and sea-surface temperature (**d, h**) during June-July-August-September (JJAS). Proxy sites discussed in the text are depicted as follows: Mawmluh Cave speleothem $\delta^{18}O$ (green triangle), SO188-KL342 (purple circle), SK237-GC04 (brown circle), Site U1446 (this study; yellow star).